JRC Scientific and Technical Reports

Benchmark Analyses for Fracture Mechanics Methods for Assessing Sub-Clad Flaws

NESC-VI Final Report

D. Lauerova [a], N. Taylor [b], V. Pistora [a], P. Minnebo [b], E. Paffumi [b]

[a] Nuclear Research Institute, Řež; [b] Institute for Energy, Petten - Ispra

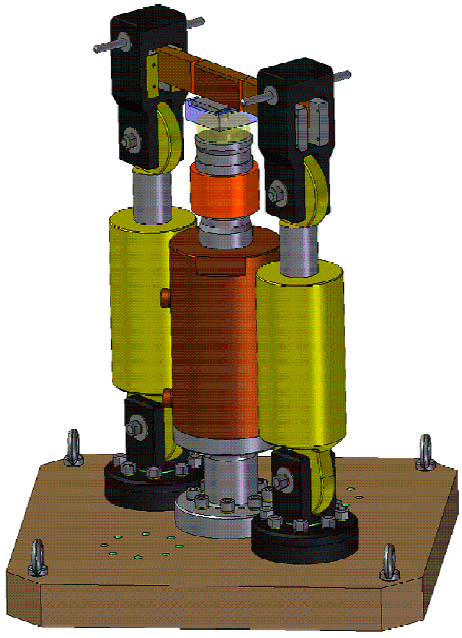

EUR 23968 EN - 2009

JRC EUROPEAN COMMISSION

Institute for Energy

The mission of the Institute for Energy is to provide support to Community policies related to both nuclear and non-nuclear energy in order to ensure sustainable, secure and efficient energy production, distribution and use.

European Commission
Joint Research Centre
Institute for Energy

Contact information

N. Taylor

Address: Via E. Fermi 1 - 21027 Ispra (VA) - Italy
E-mail: nigel.taylor@ec.europa.eu
Tel.: +39 033278 3604

http://ie.jrc.ec.europa.eu/
http://www.jrc.ec.europa.eu/

JRC 52275

EUR 23968 EN

Luxembourg: Office for Official Publications of the European Communities

Printed in The Netherlands

CONTENTS

EXECUTIVE SUMMARY

The sixth project of the Network for Evaluating Structural Integrity (NESC-VI) deals with the fracture mechanics analysis of a set of 3 tests on beam specimens with simulated sub-surface flaws, which were performed by NRI Řež plc for the PHARE project "WWER Cladded Reactor Pressure Vessel Integrity Evaluation (with Respect to PTS Events)". The objectives were as follows:

- to assess the capability to predict whether the cracks propagating into the cladding arrest or cause full fracture, and
- to assess the capability to predict the location of first initiation: near-surface or deep crack tip.

The project was launched in December 2006 and completed in March 2009. It brought together a group of 10 organisations from NESC to perform comparative analyses of selected tests, based on a comprehensive data-pack prepared by NRI. The investigations focussed almost exclusively on assessing the capability to predict the location of first initiation. The main results are as follows:

- Comparison of analyses performed by individual partners showed that the FE simulations produced consistent predictions of the observed force vs. load-line displacement (or crack mouth opening displacement) behaviour. However the differences in predicted crack tip stress intensity, K_J, as a function of applied loading were greater than those found in similar intercomparisons made as part of previous NESC projects. This underlines the importance of periodically performing such exercises.
- The influence of two modelling factors on K_J was clearly established: firstly for this type of specimen, for which the clad makes up almost 12% of the cross-section, the associated residual stresses have a significant effect in reducing K_J values and therefore need to be considered in "best-estimate" analysis. The second concerns the use of 2-D or 3-D models: in this case the 2D FE models underestimated K_J values and are considered non-conservative.
- For this combination of test specimen geometry and flaw, constraint loss is expected at the near-surface tip. A range of constraint parameters were evaluated (elastic T-stress, elastic-plastic T-stress and Q) to confirm this. However only in two cases these were used in quantitative analyses: constraint-modified FAD and K_{Ieff}, both using elastic T-stress. These indicate that fracture is likely to initiate at lower (deep) tip, which is consistent with the limited high-speed video camera evidence. In general more systematic application of 2-parameter approaches is needed.
- Both local approach models predicted initiation of cleavage fracture first from the lower crack front for medium and higher loads.

Concerning the capability to predict whether the cracks propagating into the cladding arrest or cause full fracture, the two analyses performed indicate that when the load at first pop-in is low, crack arrest in the clad can be correctly predicted on the basis of the J-R curve, but that further work is needed to ensure the reliability of such approaches over the full load range.

ABBREVIATIONS AND SYMBOLS

ASTM	American Society for Testing and Materials
BM	Base Metal
°C	Degree Celsius
CMOD	Crack Mouth Opening Displacement
EDM	Electro-Discharge Machining
FAD	Failure Assessment Diagram
FE	Finite Element
LA	Local Approach
LLD	Load Line Displacement
MC	Master Curve
NESC	Network for Evaluating Structural Components
NPP	Nuclear Power Plant
PTS	Pressurized Thermal Shock
RPV	Reactor Pressure Vessel
PWR	Pressurised Water Reactor
SSY	Small Scale Yielding
WWER	Russian-design Water-Water Energetic Reactor
a	crack depth
Δa	amount of crack growth
ε	strain
E	Young's modulus
K_J	elastic-plastic equivalent stress intensity factor or crack driving force (calculated from J)
K_{Ic}	linear-elastic plane-strain fracture toughness
J	J-integral
ν	Poisson's ratio
σ	stress
σ	standard deviation for T_0
σ_y	yield strength
σ_0	yield strength
σ_f	flow stress
σ_w	Weibull stress
σ_u	parameter of Weibull distribution (scaling stress)
$\sigma_{w,min}$	minimum Weibull stress for cleavage fracture
F	total force
m	Weibull modulus
M	moment
Q, Q_H	crack tip constraint parameters
$R_{p0.2\%}$	yield strength
R_m	tensile ultimate strength
T	T-stress
T	specimen temperature
T_0	Master Curve reference temperature

1 INTRODUCTION

The sixth project of the Network for Evaluating Structural Integrity (NESC-VI) deals with the fracture mechanics analysis of a set of 3 tests on beam specimens with simulated sub-surface flaws, which were performed by NRI Řež plc for the PHARE project "WWER Cladded Reactor Pressure Vessel Integrity Evaluation (with Respect to PTS Events)". The objectives were as follows:

(1) to assess the capability to predict whether the cracks propagating into the cladding arrest or cause full fracture, and

(2) to assess the capability to predict the location of first initiation: near-surface or deep crack tip.

The project was launched in December 2006 and completed in March 2009. It brought together a group of 10 organisations from NESC to perform comparative analyses of selected tests, based on a comprehensive data-pack prepared by NRI. This report provides a summary of the work performed and the main findings.

2 PROJECT BACKGROUND

2.1 Fracture Mechanics Issues for Sub-Clad Flaws

For light water reactors the integrity of the Reactor Pressure Vessel (RPV) has to be demonstrated for severe overcooling transients, considering also that crack-like flaws could be present in the vessel wall [1]. For safety assessment purposes such postulated flaws are generally assumed to be surface breaking, located on the inner clad surface and of semi-elliptical form. Studies on actual defect distributions indicate that actual RPV flaws, if present at all, are more likely to be sub-surface [2]. This has prompted a series of studies aimed at optimising the fracture mechanics procedures for evaluating brittle fracture initiation at such flaws. Such procedures need however to be properly validated against experimental data, and while several previous NESC projects have included sub-clad flaws, NESC-VI focuses on the role played by the stainless cladding at the inner surface of a WWER-type vessel if fracture were to initiate at a postulated sub-surface flaw.

2.2 PHARE Project "WWER Cladded Reactor Pressure Vessel Integrity Evaluation (with Respect to PTS Events)"

The objective was to prepare and validate, through adequate experiments, a procedure for the integrity evaluation of WWER reactor pressure vessels with the presence of austenitic cladding, mainly with respect to PTS events. One of the main activities was a series of 11 semi-large scale experiments on specimens containing underclad (embedded) cracks, performed at NRI Řež over the period 2005/6. The goal was to determine fracture properties of RPV samples with cladding and to select proper failure criteria to be used in RPV integrity evaluation. Initially the project reports were confidential to the project participants, although selected results have recently been presented in international conferences [3], [4], [5], [6].

2.3 The NESC Network

The Network for Evaluating Structural Components (NESC) was launched in 1992 to promote and manage collaborative international projects that focus on validating the entire process of structural integrity assessment. NESC has worked over the last 10 years to:

- create an international network to undertake collaborative projects capable of validating the entire structural integrity process;
- support development of best practices and the harmonisation of standards;
- improve codes and standards for structural integrity assessment and to transfer the technology to industrial applications.

The network [7] brings together some 30 operators, manufacturers, regulators, service companies and R&D organisations in semi-scale experimental projects. It is operated by the European Commission's Joint Research Centre (JRC) as part of a family of European networks [8]. Table 1 lists the main projects. NESC-VI is the final project run by NESC as an independent network, and future activities will be performed as part of the NULIFE network of excellence [9].

In NESC the set of coordinated experimental and analytical studies making up each project were funded primarily through so-called "in-kind" contributions, whereby participating organisations contribute work and are then entitled to have access to the contributions of others to any given project. Members have also benefited from the shared cost actions of the European Commission's Research Framework Programmes and in many cases these small dedicated research projects were pilot or seed projects for subsequent larger network-supported actions.

Table 1 NESC Network Projects.

Project	Benchmark Test(s)	Duration
NESC-I Spinning cylinder [10]	Spinning cylinder pressurised thermal shock (PTS) test performed by AEA Technology in March 1997 (main test sponsor HSE)	1993-2001
NESC-II Brittle crack initiation, propagation and arrest of shallow cracks in a clad vessel under PTS loading [11]	Two PTS tests on cylinders with shallow cracks performed by MPA Stuttgart in 2000/2001	1999-2003
NESC-III Integrity of dissimilar metal welds [12]	Large-scale test on a dissimilar weld pipe assembly (performed by EDF, as part of ADIMEW)	2001-2006
NESC-IV [13] Investigation of the transferability of Master Curve technology to shallow flaws in reactor pressure vessel applications	Biaxial bend tests on large cruciform-type test pieces with surface semi-elliptic defects and uniaxial bend tests on beams with sub-surface flaws (performed by ORNL)	2001-2006
NESC-TF Thermal Fatigue [14]	Database of thermal fatigue data for operating components and mock-ups	2003 - 2006
NESC-VI	Analysis of the NRI PHARE embedded flaw tests	2006-2009

2.4 NESC-VI Objectives and Organisation

The project objectives were as follows:

(1) to assess the capability to predict whether the cracks propagating into the cladding arrest or cause full fracture, and

(2) to assess the capability to predict the location of first initiation: near-surface or deep crack tip.

The work was launched in December 2006 with the release of the data-pack [15] and completed in March 2009. Table 2 shows the project milestones and schedule. Ten organisations took part, as listed in Table 3. Their main tasks were to perform comparative analyses of the three selected tests, based on the data prepared by NRI. The project relied on in-kind i.e. un-funded, contributions, following the established system for NESC network projects. The project leadership was provided by NRI, while the JRC, as NESC Operating Agent, coordinated the work. Progress was reported to the 6-monthly NESC Steering Committee meetings, who also have final approval of all documents released by the network. The documentation including minutes of meetings, test results, analyses and the main reports are stored in the NESC archive and are available electronically via the JRC's DOMA site: http://odin.jrc.nl/doma.

Table 2 Milestones in the NESC-VI Project.

Date	Event/Action
2005	PHARE Tests
December 2006	NESC-VI Launch
2006	Distribution of Data-Packs
November 2007	Progress Meeting
July 2008	Draft Report
December 2008	Report Approved by NULIFE Steering Committee

Table 3 Participating organisations.

Organisation
AREVA NP GmbH, Germany
Bay Zoltan Foundation, Institute for Applied Logistics, Hungary
British Energy Ltd.
European Commission, Joint Research Centre, Institute for Energy
Fraunhofer Institut für Werkstoffmechanik, Germany
Inspecta Technology AB, Sweden
Nuclear Research Institute Řež plc, Czech Republic
ORNL, USA
Tractebel, Belgium
VTT, Finland

3 THE PHARE EMBEDDED FLAW TESTS

3.1 Test Materials

To be representative of WWER-440 reactor pressure vessels, archive material from a decommissioned reactor pressure vessel was chosen. The base metal (BM) and the cladding had both been manufactured with the same technology as used for the vessels in Dukovany NPP. Blocks with dimensions of approximately 500 mm x 1000 mm were mechanically cut from the vessel; taking also the full thickness of the austenitic cladding. The blocks were then heat treated by a special procedure to obtain a similar degree of embrittlement (defined by the ductile-to-brittle transition temperature) as an RPV at the end of its design lifetime.

3.1.1 Tensile properties

For both the thermally treated (aged) BM and cladding, three tensile tests at room temperature were performed on small round tensile specimens with diameter 4 mm. Results obtained from one selected tensile test (for each of the two materials) were mathematically treated to obtain the true stress - true plastic strain curve, see Figure 1 and Figure 2. The elastic and strength properties are summarized in Table 4:

Table 4 Mechanical properties of the aged base and clad materials.

Material	**E GPa**	**υ**	**$R_{p0.2}$ MPa**	**R_m MPa**
Aged BM	211	0.3	887.8	984.1
Aged cladding	162	0.3	337.9	593.9

3.1.2 Fracture Toughness

The master curve reference temperature T_0 was determined for aged BM, based on samples taken from two locations: 3 mm below BM–cladding interface and 18 mm below BM–cladding interface. Pre-cracked Charpy specimens loaded by three-point-bending were used. The respective T_0 values together with their standard deviations as determined according to ASTM-1921 are:

- at 3 mm below the interface: T_0 = 22.8 °C, σ = 5.4 °C
- at 18 mm below the interface: T_0 = 19.0 °C, σ = 5.7 °C

3.1.3 J-R curves for the cladding

The J-R curves were determined both for the 1st and the 2nd layer of the cladding (ss-1 and ss-2). Three specimens were tested for each layer. The following lower bound curves were established:

- for the 1st layer: $J = 590.da^{0,5}$
- for the 2nd layer: $J = 180.da^{0,7}$

where *da* is in mm, J is in $kJ.m^{-2}$.

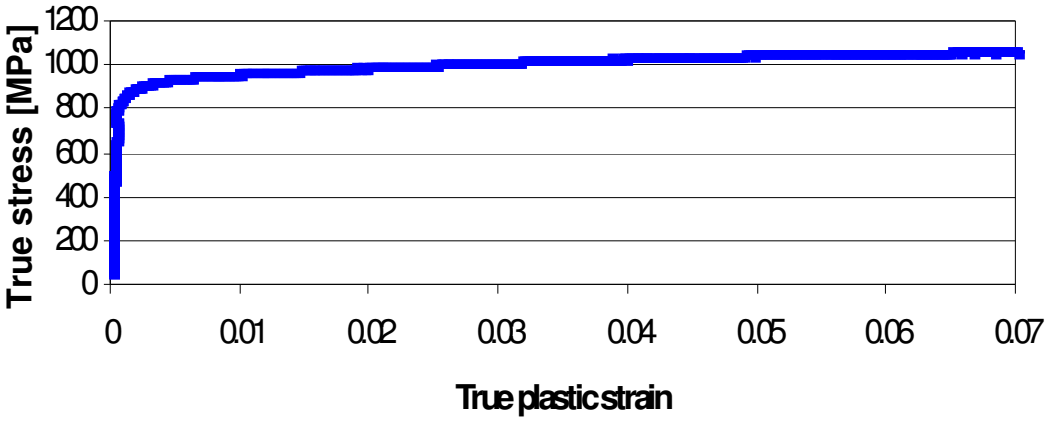

Figure 1 True stress-strain curve at RT for artificially aged base metal.

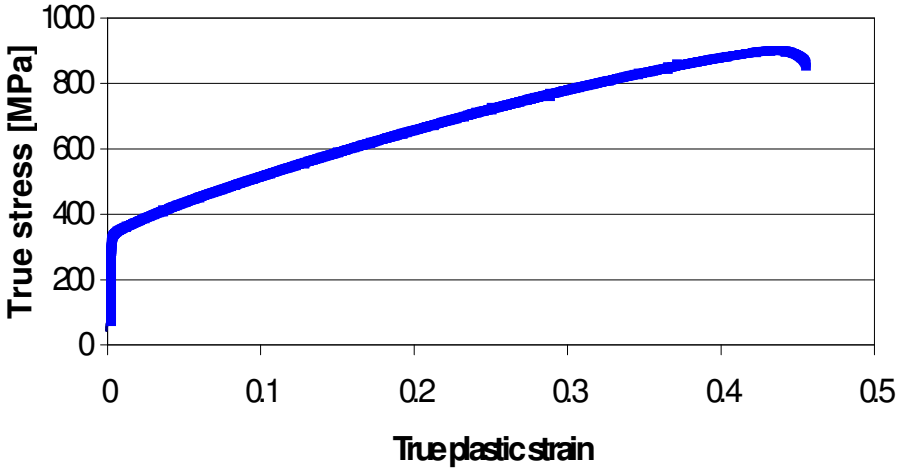

Figure 2 Tensile properties for thermally treated cladding at RT.

3.1.4 Residual Stresses

The beam thinning method was applied to measure the residual stresses in the specimens. This consists in step-by-step milling of layers of material from one side of a beam specimen, while on the other side a strain gauge is installed; after cutting-off of any individual layer, strain (in longitudinal direction of the specimen) is measured. A formula taken from literature for calculation of residual stresses in the positions of individual layers based on measured strains and Young's modulus was applied after the measurement. The method can only measure the component of stress oriented in the same direction as the specimen length.

The dimensions of the specimens used for measurement of residual stress were 200x10x35 mm (35 mm was the total thickness, of which 10 mm was cladding and 25 mm base material). The cutting-off process started on the upper cladding surface and continued towards the bottom (base material) surface of the specimen.

Specimens for two material states were tested: as-received (directly taken from the RPV) and artificially aged (by quenching and tempering); the latter was used for semi-scale fracture tests. Specimens of two orientations were manufactured from both blocks: axial and circumferential with respect to vessel wall. Due to the circumferential direction of the austenitic cladding welding process, the specimen with axial orientation was used for determination of the transversal residual stress (with respect to cladding bands), while the specimen with circumferential orientation was used for determination of the longitudinal residual stress (with respect to cladding bands).

Combining these possibilities, four types of specimens were used (as received and aged conditions, axial and circumferential orientations). For each, four specimens were tested, the results averaged and finally the average residual stress variation over specimen width was obtained (Figure 3).

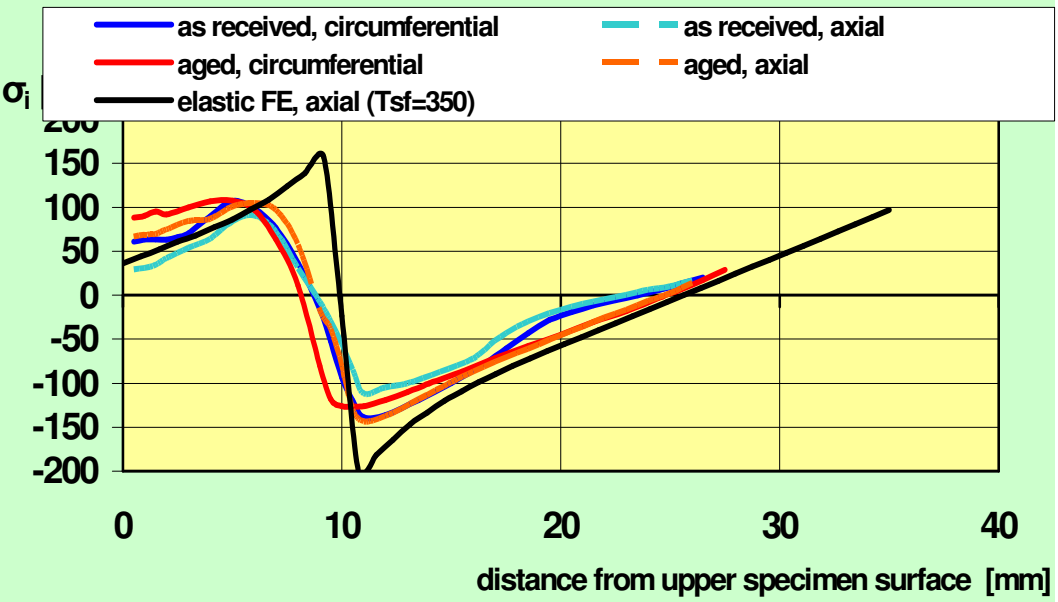

Figure 3 Variation of measured residual stresses near BM-cladding material interface (for comparison, the FE result for a stress free temperature of 350°C is included).

3.2 Embedded Flaw Specimens

The test beams for four-point bending had cross-section nominal dimensions of 40 x 85 mm, including cladding. The design and loading arrangement is shown schematically in Figure 4. Inserts from archive materials with the length of 200 mm were welded together with the arms to obtain a final required length of 670 mm. Two types of sub-surface through-crack geometries were tested:

- "Normal" specimens with a crack height of 15 mm and with the upper tip located 3 mm under the interface between the cladding and the base material (Figure 5a). Both crack tips were fatigue sharpened. The specimen codes were 1E2, 1E3, 1E4, 1E5, 1E9, 1E10, 1E11 and 1E12.

- So-called “abnormal” specimens with sub-surface cracks of depth 40 mm and the upper tip located 3 mm under the clad-base material interface (Figure 5b). In this case only the upper crack tip was sharp, the lower crack tip having been artificially blunted (drilled out). These specimens were marked 1E6, 1E7 and 1E8.

Precise measurements were made of the actual defect dimensions after each test from digital photos of the opened surfaces. Examples are shown in Figure 6 and Figure 7.

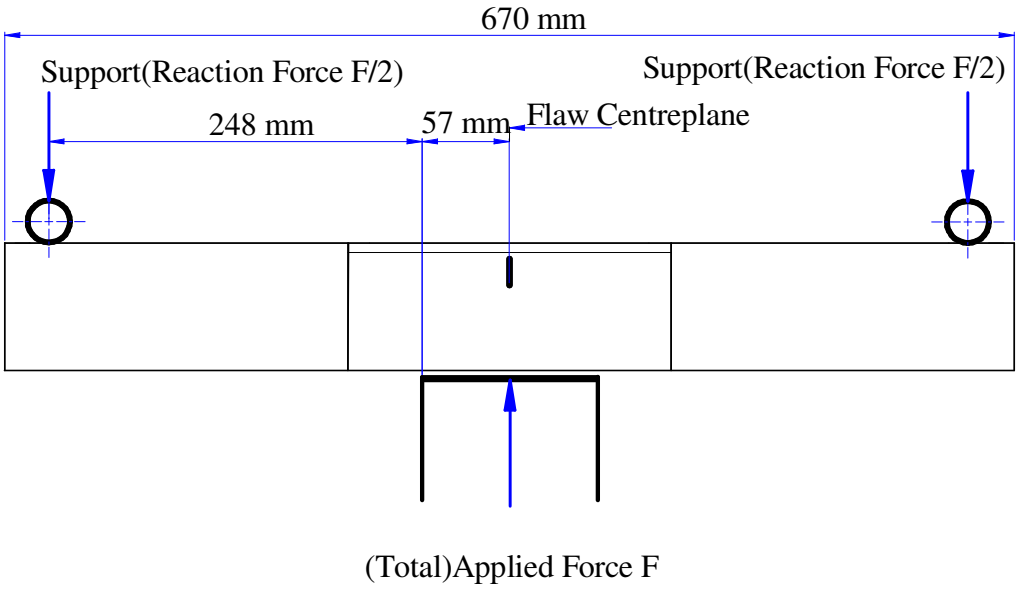

Figure 4 Beam and loading system dimensions (normal specimen shown).

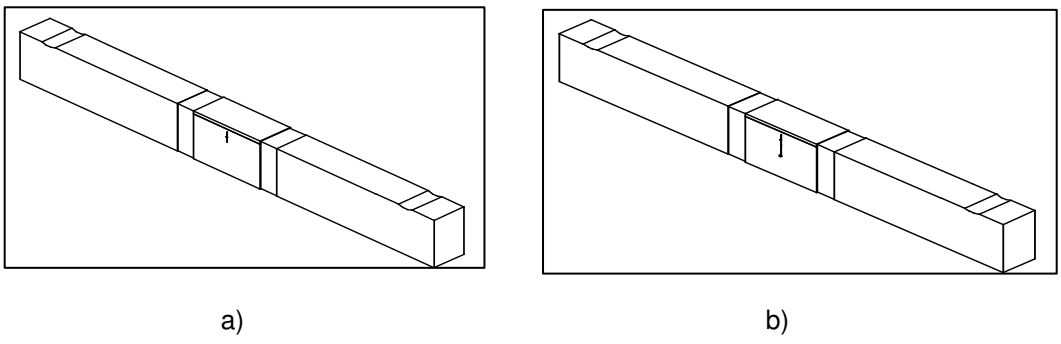

Figure 5 Sketch of a) the normal specimen (20 mm high flaw) and b) the “abnormal” specimen (extended 40 mm high flaw).

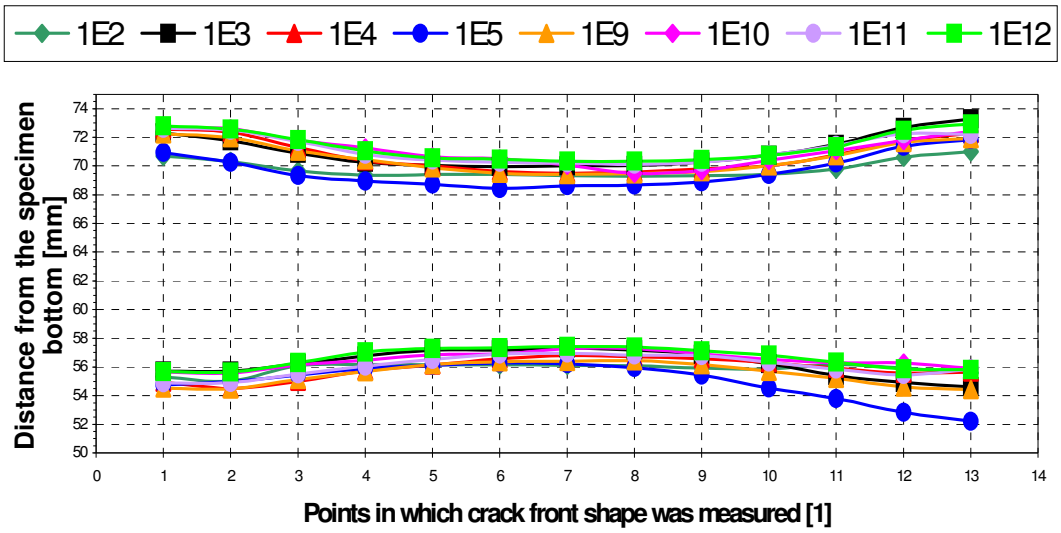

Figure 6 Crack front shapes, for both upper and lower crack fronts, for normal specimens.

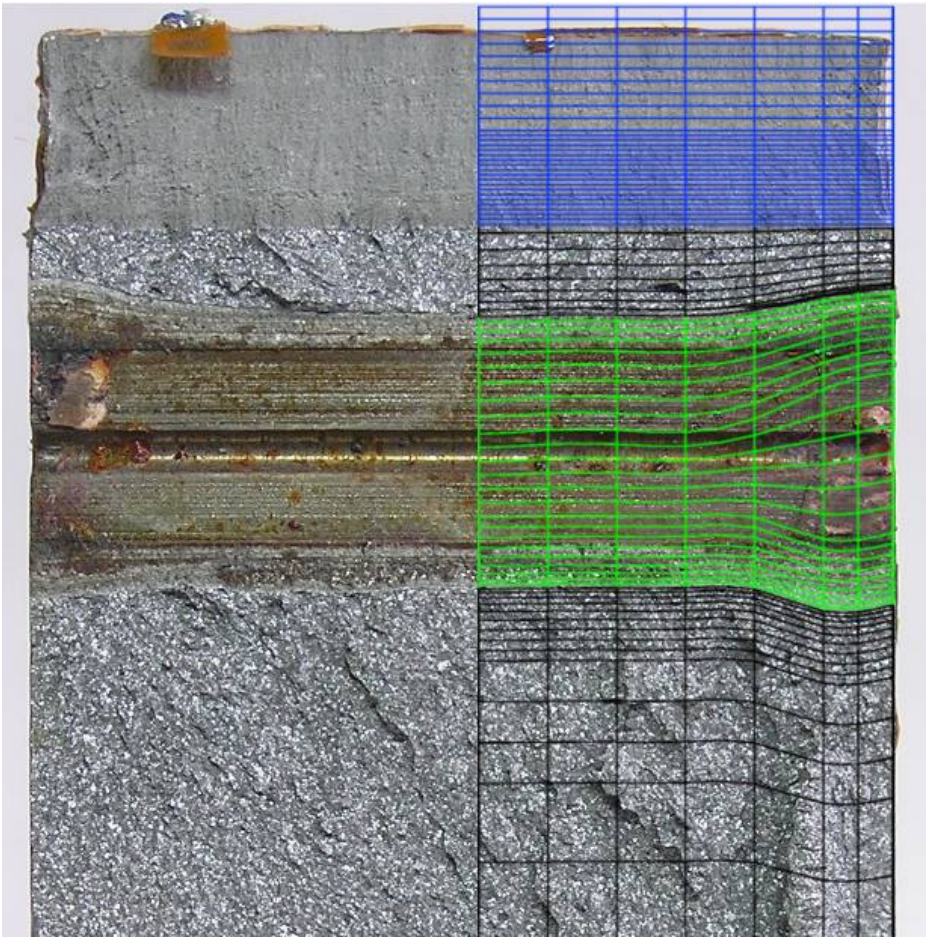

Figure 7 Detail of the 1E2 fracture surface showing the curvature of the crack front towards the sides of the specimen after pre-cracking, and a corresponding FE mesh.

3.3 Test Equipment and Procedure

A diagram of the experimental equipment is given in Figure 8. The beam-type specimen is located on the central mast, centred by a fastener. The two outer hydraulic cylinders with the same piston area serve as reaction columns; the loading is applied via the central hydraulic cylinder, with a maximum force of 1 MN.

The beams were pre-loaded to approximately 5 kN to facilitate the test preparation. Pre-loading and further loading was controlled by a servo system that initiated a tension of piston in the central cylinder with respect to base plate through forks, pins and sleeves. The test beam was loaded over two edges symmetrically located in the distance equal to 57 mm from transverse central axis. Thus, in the area of the central part of the specimen where the defect is located, there is a constant bending moment along the whole length of specimen between the supporting edges. The distance between symmetrical loading locations and supporting edges is 248 mm (Figure 4); the maximum bending moment was 124 kNm. On account of the high level of energy accumulated during loading, the rig is equipped with a safety cage designed to catch any parts that come loose during loading.

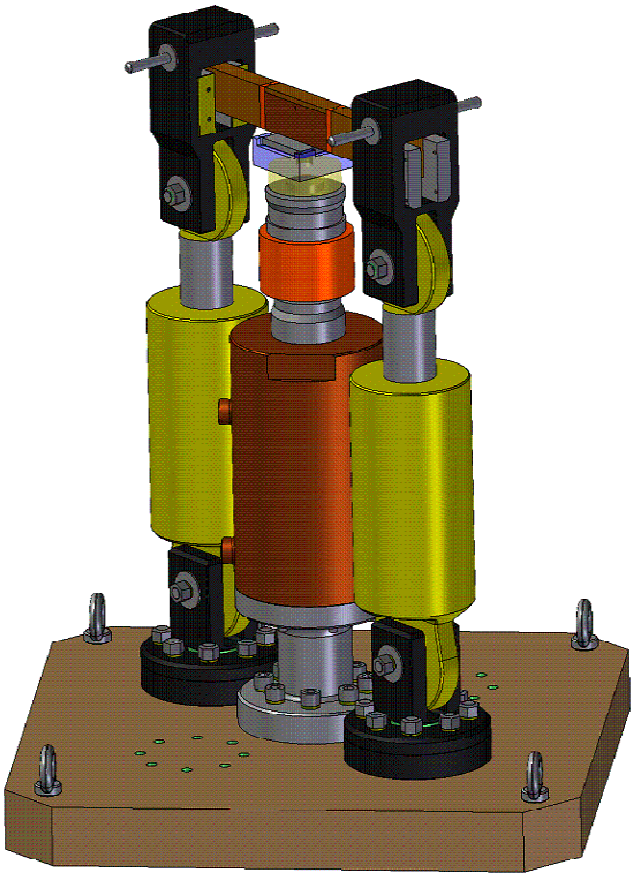

Figure 8 Scheme of experimental equipment.

The whole loading system, the positioning of the beam via the central fastener, the precise application of loading forces and other features of the equipment ensured repeatable testing conditions.

Specimen Dimensions:

length	670 mm (distance between supporting lines is 610 mm)
width[1]	40 mm
thickness[1]	85 mm incl. cladding

Control of test equipment:

The test equipment was equipped with independent control and measuring units, with an external generator of loading and external measuring units for individual transducers of force and displacement. Loading during the tests was controlled by the displacement of loading piston up to the fracture, at a rate that can be varied.

Temperature:

All the tests were conducted at room temperature (19 to 23°C).

Testing Procedure:

Beam-type specimens contained a crack type defect obtained by fatigue loading of an initial EDM notch. The test procedure was as follows:

1. Identification and measurement of the specimen, identification of loading and fracture parameters.
2. Mounting of the specimen in the test equipment, pre-loading to approximately 5 kN (the precise value is recorded), installation of measuring devices.
3. Slow quasi-static loading up to specimen fracture or pop-in; if pop-in occurred, the test was interrupted for some time for documentation, photos etc., and then loading continued up to final fracture. The specified measurement parameters were continuously recorded. A test lasted between 10 and 40 minutes.
4. Treatment of the fracture surfaces against corrosion, identification and marking of the broken arms, cutting-off of the fracture surfaces and fractography.
5. A database of raw measured parameters was created - data were archived on CD as files marked in a similar manner as the specimens.

During the test the following parameters were measured and recorded:

F [kN]	total applied force in the central mast
LLD [mm]	Load Line Displacement: movement of the piston with respect to the base plate was measured (for all specimens)
CMOD [mm]	Crack Mouth Opening Displacement, measured on the flank surface of the specimen, approximately in the middle of crack depth (only for abnormal specimens). CMOD-meter was calibrated up to 2.5 mm (accuracy approx. 0.3 %)
T [^{o}C]	specimen temperature

[1] Width here means the specimen dimension perpendicular to direction of crack front propagation, and thickness means the specimen dimension parallel to direction of crack front propagation.

All transducers were calibrated together with the measuring apparatus; measured data have been evaluated by a measuring unit controlled by PC.

3.4 Results

NRI tested a total of 8 normal and 3 abnormal specimens (Table 5). Three of the normal specimens failed suddenly (fractured through) after initiation of brittle fracture, while the five remaining normal specimens exhibited pop-ins both at the near-surface tip, with crack arrest in the cladding close to cladding-base material interface, and at the deep tip with crack arrest in the base material close to the bottom of the specimen. The force values just before pop-in for these specimens were lower than in case of the specimens that fractured through. During the subsequent loading, additional pop-ins as well as ductile tearing in the clad was observed, before final specimen failure. All 3 abnormal specimens exhibited initiation of brittle fracture (pop-in) from the upper crack tip, crack arrest in the cladding and some ductile tearing into the cladding during subsequent loading, before the final specimen failure. As intended there was no crack propagation from the blunted bottom tip.

Table 5 Summary results of the full set of PHARE tests.

Specimen No.	Specimen Type	Average crack length	Test temper.	Max. force	Force after 1st pop-in	Failure features
		(mm)	(ºC)	(kN)	(kN)	
1E2	normal	13,8	20,5	259,7	110	pop-in to cladding, subsequent pop-ins
1E3	normal	14,6	21	202,8	122	pop-in to cladding, several subsequent pop-ins
1E4	normal	14,7	20,5	339,4	-	sudden fracture through
1E5	normal	14,4	21	283,2	63	pop-in to cladding, later fracture through
1E9	normal	14,9	23	315,7	-	sudden fracture through
1E10	normal	14,5	22	305,9	-	sudden fracture through
1E11	normal	15,0	21	278,1	110	pop-in to cladding, subsequent pop-ins
1E12	normal	14,6	21,5	220,7	177	pop-in to cladding, several subsequent pop-ins
1E6	abnormal	39,6	21,5	195,8	151	pop-in to cladding, later fracture through
1E7	abnormal	39,7	19,5	205,5	162	pop-in to cladding, later fracture through
1E8	abnormal	39,7	21,7	197,3	152	pop-in to cladding, later fracture through

The following three specimens were selected for the NESC-VI studies:
1E2 – normal specimen with pop-in
1E4 – normal specimen with sudden through-fracture
1E7 – abnormal specimen with pop-in

Figure 9 shows the experimental total force vs. LLD curves from the 3 selected tests. Figure 10 shows the experimental force vs. CMOD curves for specimen 1E7 (there are two curves since measurements was performed on both flanks of the specimen). Table 6 summarises the test results, such as load at initiation of fast fracture and load after first pop-in (for cases with crack arrest), crack dimensions, etc. Note that for the normal specimens, the first pop-in into the cladding occurred simultaneously with pop-in into the base material at the lower tip. The remaining ligaments in the base material after first pop-in varied between the specimens;

essentially, the larger was the force before first pop-in, the smaller the remaining ligament.

During some of the experiments a video camera recording was made of the surface in an attempt to detect which crack front initiated first. Two high-speed video cameras were used for this purpose, and at least in two cases, specimens 1E9 and 1E11, cleavage fracture initiation was found to begin at the lower crack front.

Table 6 Detailed results of the tests selected for analysis in NESC-VI.

Spec. no.	Specimen type	Average crack length (depth) (mm)	Cladding thickness (mm)	Test temp. (°C)	Max. force (kN)	Force after 1st pop-in (kN)	Ductile tearing before 1st pop-in (mm)	Bottom ligament after 1st pop-in (mm)
1E2	normal	13.8	10.8	20.5	259.7	110	0.045	~5
1E4	normal	14.7	11.3	20.5	339.4	-	0.133	-
1E7	abnormal	39.7	11.2	19.5	205.5	162	0.342	31

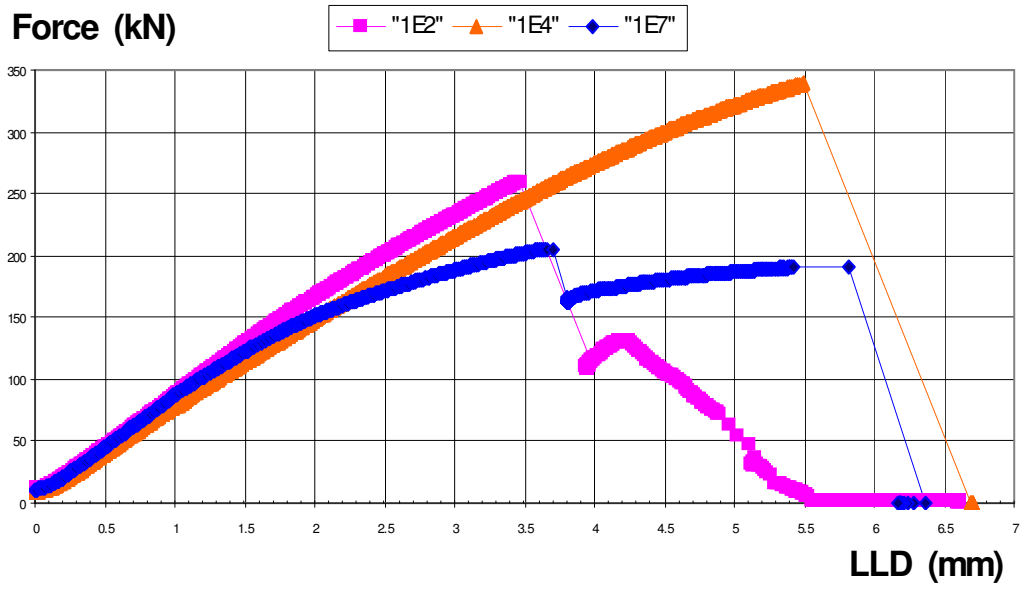

Figure 9 Experimental force vs. LLD curves for specimens 1E2, 1E4 and 1E7.

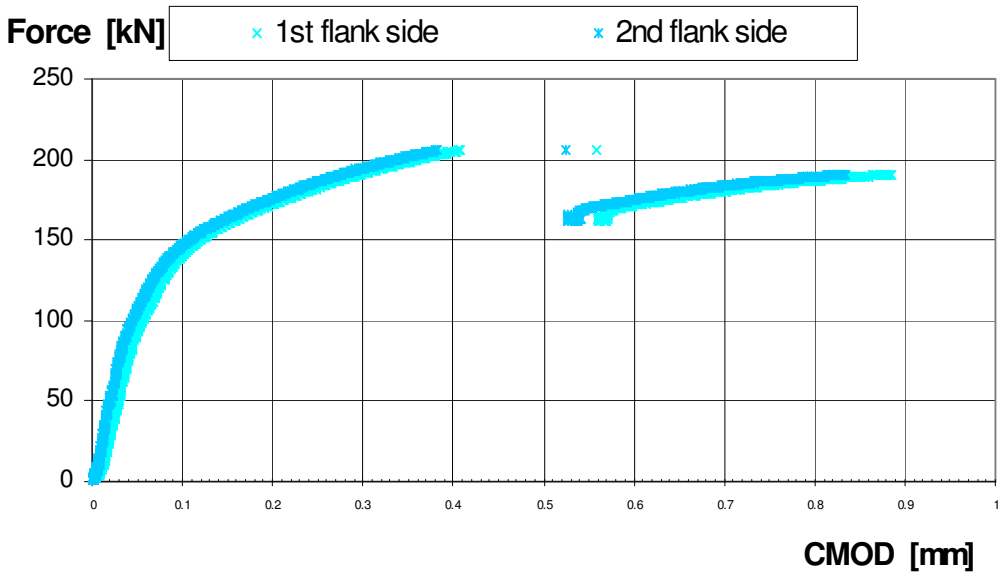

Figure 10 Experimental force vs. CMOD curve for specimen 1E7.

3.5 Fractographic Analysis

The post-test fractographic analyses focussed on the ductile tearing before cleavage fracture as well as on identification of crack front position after pop-in. The results for the three specimens selected for NESC-VI are summarised in Table 7. It proved impossible to identify the crack front position in the cladding after the pop-in (crack arrest).

The results of the detailed fractographic examination of specimen 1E2 are given in Annex A. It was found that the crack propagation mode changes from transgranular cleavage fracture in the BM to brittle intergranular fracture in a very narrow layer in the BM close to the BM-clad interface, then into ductile intergranular fracture in a very narrow layer in the cladding close to BM-clad interface, and finally into ductile transgranular fracture in areas of both 1st and 2nd cladding layers.

Table 7. Fractography results of the tests selected for analysis in NESC-VI.

Spec No.	Specimen Type	Ductile tearing before 1st pop-in (mm)	Remark	Bottom ligament after 1st pop-in (mm)	Failure features
1E2	normal	0,045	blunting	~5	1 mm pop-in to cladding, subsequent pop-ins
1E4	normal	0,133	blunting + tearing	-	sudden fracture through
1E7	abnormal	0,342	blunting + tearing	31	pop-in to cladding, later fracture through

4 STRESS AND FRACTURE ANALYSIS

4.1 Introduction

Nine organisations contributed results of the NESC-VI stress and fracture analyses, as shown in Table 8. Section 4.2 below provides a brief description of the individual analyses, while section 4.3 compares the values obtained for key parameters.

Table 8 Overview of stress and fracture analyses of the NESC-VI tests.

Organisation		Analysis Type	Report/Source
1	ORNL	local approach analysis, calculation of constraint parameters	Report 6/11/2007, Yin and Williams
2	AREVA NP GmbH	local approach analysis	Report Feb 2008, Hümmer & Keim
3	British Energy	R6 methods, including constraint options	Presentation Nov. 2007, Smith
4	Inspecta	2D and 3D analyses, in which the crack driving forces and the crack-tip constraints are evaluated	Report Feb. 2007, Sattari-Far
5	Tractebel	elastic + elastic-plastic calculations, J-integral	Report 17/3/2008, Malekian
6	Fraunhofer IWM	FE calculations of the crack initiation and arrest behaviour	Presentation Nov. 2007, Siegele & Varfolomeyev
7	VTT	Abaqus FE code (version 6.7-1), calculation of the crack initiation	Presentation June 2007, H. Keinanen
8	Bay Zoltan Institute for Applied Logistics	J-calculations using MARC	1. "Report for assessment of sub-clad flaws, J-integral calculation for NESC-VI project", Szabolcs Szávai and Róbert Beleznai, September 2007 2. "Study of increased crack sizes of sub-clad flaws, J-integral calculation", Szabolcs Szávai and Róbert Beleznai, January 2008
9	NRI	FE analyses of driving force and constraint parameters	1. NRI Phare reports 2. Collation of NESC-VI analyses

4.1.1 Stress Intensity Factor and Constraint Parameters

Concerning the crack tip behaviour, the focus in the first instance is on the stress intensity factor K_J, which is calculated from the FE-computed J value using the standard plane-strain conversion formula:

$$K_J = \sqrt{\frac{E.J}{1-\nu^2}} \qquad (1)$$

Several investigations examined the role of constraint, focusing on parameters such as T-stress and Q. These may be used in the so-called two-parameter approaches: K-T, K-Q, K-Q_H etc.

a) T-stress

The asymptotic expansion of the stress field near a sharp crack in a linear elastic body is

$$\sigma_{ij} = \frac{K_I}{\sqrt{2\pi r}} f_{ij}(\theta) + T\delta_{1i}\delta_{1j}, \qquad (2)$$

where r and θ are the in-plane polar coordinates centred at the crack tip. The local axes are defined so that the 1-axis lies in the plane of the crack at the point of interest on the crack front and is perpendicular to the crack front at this point; the 2-axis is normal to the plane of the crack (and thus is perpendicular to the crack front); and the 3-axis lies tangential to the crack front. The T-stress represents a stress parallel to the crack faces.

b) Q-parameter

The Q parameter is expected to provide a more accurate estimate of constraint level than the T-stress at loads for which elastic-plastic conditions prevail. The formulation of Q is frequently based on the crack opening stress, σ_1:

$$Q = \frac{\sigma_1 - (\sigma_1)_{SSY,T=0}}{\sigma_0}, \qquad (3)$$

where $(\sigma_1)_{SSY,T=0}$ is the stress opening the crack for the small-scale yielding (SSY) solution with T-stress = *0* and σ_0 is the reference stress in the Ramberg-Osgood material model. These stresses are evaluated at a distance $r = 2J/\sigma_o$ ahead of the crack tip. An alternative Q-stress definition uses the hydrostatic stress and is considered sensitive to out-of-plane loading (this is particularly relevant to the biaxial loading which occurs during PTS transients).

4.1.2 Local Approach

In this paragraph, a description of the procedure that may be recommended for constructing the predicted cumulative failure probability P_f is described, if the low and high constraint experimental data are not available and only one value of Master Curve reference temperature T_0 is known.

The local approach is an alternative to K-based methods and is based on the Beremin Weibull methodology [19] that employs a multi-axial form of the *weakest-link* model applicable for a 3-D cracked solid. The Weibull stress, σ_w, is characterized as a fracture parameter reflecting the local damage of the material near the crack tip:

$$\sigma_w = \left[\frac{1}{4\pi V_0} \int_{\Omega} \int_0^{2\pi} \int_0^{\pi} \sigma_q^m \sin\varphi \, d\varphi \; d\theta \; d\Omega \right]^{\frac{1}{m}} \qquad (4)$$

It is evaluated by integration of the equivalent stress, σ_q, over the process zone. In Eq. (4), V_0 is a reference volume; m is the Weibull modulus; θ and φ are curvilinear coordinates for integration of the tensile stress; and Ω denotes the volume of the near-tip fracture process zone, defined as the volume within the contour surface $\sigma_1 \geq \lambda\sigma_0$, where σ_1 is the maximum principal stress and σ_0 is the yield stress. The cut parameter λ is nominally set to 2 to ensure that all material points within the active process zone have undergone plastic deformation. A fracture criterion must be specified to determine the equivalent (tensile) stress, σ_q in Eq. (4), acting on a microcrack included into the fracture process zone. While the crack opening stress component σ_1 is often used, for biaxial loading the hydrostatic stress criterion (where $\sigma_q = I_1/3 = \sigma_H$) provides more consistent predictions of experiments.

The cumulative probability of failure by transgranular cleavage P_f can be estimated by a three-parameter Weibull distribution of the form:

$$P_f(\sigma_W) = 1 - \exp\left[-\left(\frac{\sigma_w - \sigma_{w,\min}}{\sigma_u - \sigma_{w,\min}} \right)^m \right], \qquad (5)$$

where the parameters are the Weibull modulus m (shape parameter), the scaling stress (scale parameter) σ_u , and the minimum Weibull stress for cleavage fracture $\sigma_{w,min}$ (location parameter). The GRD calibration scheme [24] is typically used to determine unique values of the Weibull parameters (m, σ_u) using toughness data measured under low and high constraint conditions at the crack front[2].

To obtain fracture toughness data the Weibull statistical model is associated with the Master Curve methodology. According to the ASTM E1921-02 the cumulative distribution, *cdf*, for the Master Curve Weibull model has the form:

$$P_f(x \leq K_{JC}) = F(K_{JC}) = 1 - \exp\left(-\left(\frac{K_{JC} - K_{\min}}{K_0 - K_{\min}} \right)^4 \right), \qquad (6)$$

where K_{min}=*20 MPa* $m^{0.5}$ and K_0 is the scale parameter at 63.3% probability of failure. According to ASTM E1921-02 at a given test temperature, T, and for a given reference temperature T_0 the median of the Weibull distribution, $K_{J,med}$, is defined by:

$$K_{J,med} = 30 + 70\exp\left(0.019\left(T - T_0\right)\right)[MPa\sqrt{m}] \qquad (7)$$

[2] Such data were not available for NESC-VI, so assumed values of m were used.

and can be used to determine the scale parameter, K_0, given by

$$K_0 = K_{\min} + \frac{K_{J,med} - K_{\min}}{[\ln(2)]^{1/4}} [MPa\sqrt{m}] \qquad (8)$$

To obtain now a sample of data the *inversion method*, described in [23] is applied. This method is a general procedure for simulating continuous random variables with a *cdf* $F(x)$ and its well-defined inverse F^{-1}, and can produce realizations (i.e. draw samples) from a Weibull distribution. Let U be a random variable drawn from a uniform distribution P_f on the open interval (0,1). Then, under the assumption that the *cdf,* $F(x)$, is strictly monotonically increasing, the following relation can be applied:

$$P_f(F^{-1}(U) \le x) = P_f\left(U \le F(x)\right) \qquad (9)$$

This equation is easily solved for $F^{-1}(U)$ and using equation for the Weibull distribution which results in:

$$F^{-1}\left(U_{(i)}\right) = K_{Jc(i)} = K_{\min} + \left\{(K_0 - K_{\min}) \cdot \left[-\ln\left(1 - U_{(i)}\right)\right]^{1/4}\right\} [\text{MPa m}^{0.5}], \quad (10)$$

where $U_{(i)} \in (0;1)$ is a random variable from a uniform distribution. This equation is used to produce a sample of K_{Jc} data drawn (in the "SSY space") from the continuous Weibull distribution described by Eqn. (6).

The generated data (in the "SSY space") are further converted from $K_{Jc(i)}$ into J-Integral data under plane strain via

$$J_{c(i)} = \left(\frac{1000\ mm}{1m}\right)^2 \cdot \left(\frac{1kJ}{1000\ J}\right) \cdot \left(\frac{1-\nu^2}{E}\right) K^2_{Jc(i)} \left[\frac{kJ}{m^2}\right], \qquad (11)$$

where the *J*-integral values obtained are in the units [N/mm].

The stochastically-generated toughness data from the "SSY space" are then mapped out to the "spaces of shallow and deep crack tips", as shown in Fig. 12 (using suitable selected value of m[3]) and generate a set of toughness data for the shallow and deep crack tips respectively. Then the cumulative failure probability P_f can be predicted based on the procedures in ASTM E-1921 [22], Eq. 6.
(In both the "shallow and deep crack tip spaces" first the appropriate value of K_0 has to be determined, using procedure for determination of K_0 presented in [22]).

[3] Value of *m* may be determined based on engineering judgement (or a value obtained from the GRD calibration procedure performed for a similar material may be taken), but a sensitivity analysis should be made (in case that the results are too much dependent on value of *m*, this approach should not be used).

In order to predict which crack tip initiates first during the bending, it is more suitable to present the cumulative failure probability P_f as a function of bending moment than of J or K.

4.2 FE calculations of crack driving force and constraint parameters

4.2.1 NRI

NRI Řež, as the initiator of the NESC-VI project, performed structural as well as fracture mechanics FE calculations for all specimens. In NRI PHARE reports, the results concerning cleavage fracture initiation as well as simulation of ductile tearing of cladding are attached; into the NESC-VI report only those results were included that concern specimens 1E2, 1E4 and 1E7, and particularly, only results concerning cleavage fracture.

NRI Řež modelled residual stresses in the structural FE calculation in such a manner that stress free temperature, T_{sf}, was assumed to exist in the evaluated specimens; in this case, it was assumed that T_{sf} = 350 °C. Volumetric deformations corresponding to decreasing temperature from T_{sf} to room temperature were analytically calculated for both BM and cladding (with different thermal expansion coefficients for BM and cladding) and these deformations were used as input loads applied to the appropriate elements of specimen model in the first loading step of FE calculation (and were held constant during the entire FE calculation).

For evaluation of constraint, NRI Řež used the technique of effective stress intensity factor K_{Ieff} [17]. For the purpose of determination of K_{Ieff}, values of both "elastic" and "elastic-plastic" T-stress were determined. Also, J-Q loci for both upper and lower crack fronts of normal specimens were constructed. Both values of T-stress and Q-parameter values were compared with the corresponding values determined by some of the other partners.

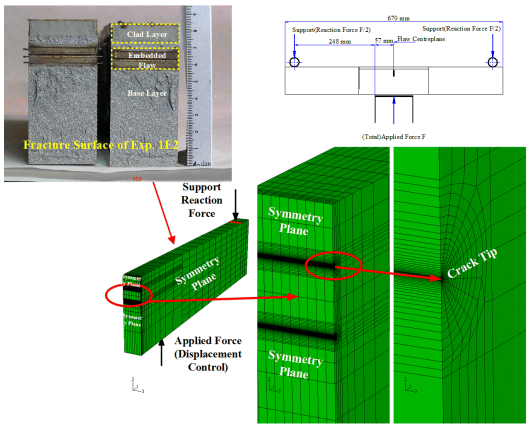

Figure 11 The ORNL quarter-section finite element model of the embedded-flaw beam under uniaxial four-point bending.

4.2.2 ORNL

ORNL contributed analyses of the constraint issues associated with embedded flaws using various fracture mechanics methods. This included application of the Weibull stress local-approach. Utilizing the symmetry conditions of the test specimen, quarter finite-element models were developed for both "normal" and "abnormal" specimens using ABAQUS/CAE version 6.6. As shown in Figure 11 a very refined mesh was defined along the shallow and deep crack-fronts to accurately calculate the stress-strain fields and driving forces around the crack tips. The finite-element models were utilized to calculate global responses of embedded flaw beams, such as Load Line Displacement (LLD) and Crack Mouth Opening Displacement (CMOD), compared with results from experiments. Various advanced fracture mechanics methods were used to quantify constraint effects due to the embedded crack, including T-Stress, Q_H stress, and the Weibull stress model.

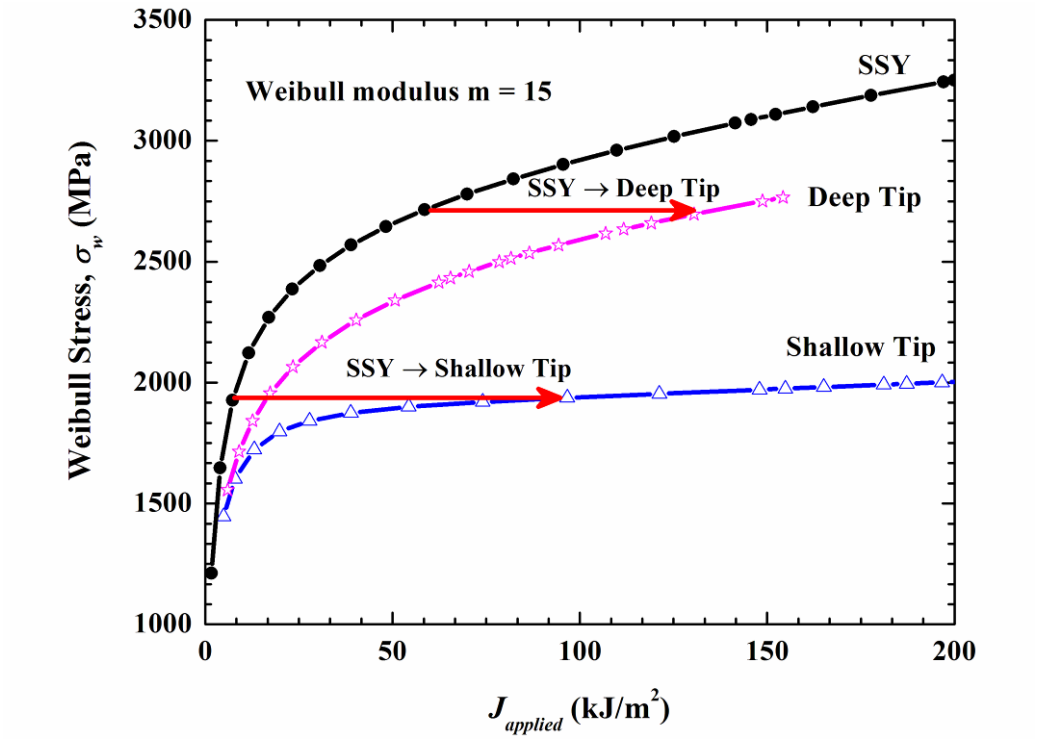

Figure 12 ORNL: Mapping the stochastically generated SSY toughness data to the shallow and deep crack tips of the embedded flaw specimen.

4.2.3 AREVA GmbH

FE simulations of the NESC-VI beam were performed for a test temperature of 20°C. The material properties were taken from [15]. Residual stresses were not taken into account. A comparison of the global FE results with experimental data showed good agreement, see Figure 13 (pop-ins were not simulated).

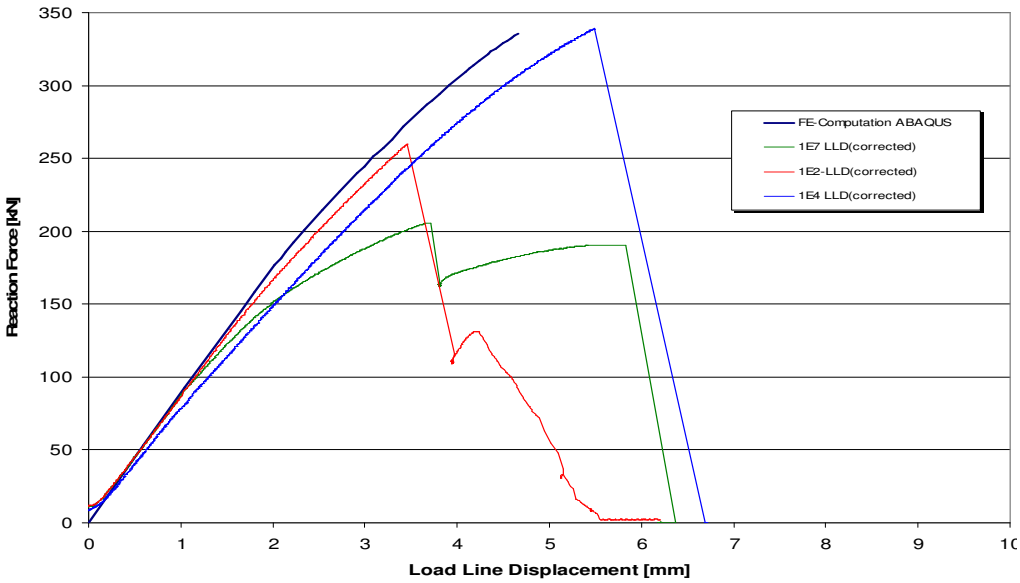

Figure 13 AREVA NP GmbH: FE results at 20°C (the green, red and light blue curves are experimental records, dark blue curve is the calculated curve).

The local approach analysis used a definition for the Weibull stress based on a conditional formulation of crack initiation and propagation. Following the formalism in [21] it is defined by:

$$\sigma_w = \begin{cases} \left(\int\limits_{V_p} \int\limits_{\varepsilon_p} \frac{\sigma_{ys}(T,\dot{\bar{\varepsilon}}_p)}{\sigma_{ys,0}} \exp\left(-\frac{\sigma_{ys}}{\sigma_{ys,0}} \cdot \frac{\varepsilon_p}{\varepsilon_{p,0}} \right) \max\{(\sigma_1^m(\varepsilon_p, dV) - \sigma_{th}^m), 0\} d\varepsilon_p \frac{dV}{V_0} \right)^{1/m} & \text{if } \sigma_1(\varepsilon_p, dV) < \max\limits_{t\in[0;T]} \sigma_1(t) \\ \left(\Sigma^m \int\limits_{V_p} \int\limits_{\varepsilon_p} \frac{\sigma_{ys}(T,\dot{\bar{\varepsilon}}_p)}{\sigma_{ys,0}} \exp\left(-\frac{\sigma_{ys}}{\sigma_{ys,0}} \cdot \frac{\varepsilon_p}{\varepsilon_{p,0}} \right) d\varepsilon_p \frac{dV}{V_0} \right)^{1/m} & \text{else} \end{cases} \quad (12)$$

where V_p is the fracture process zone, ε_p the plastic strain, $\varepsilon_{p,0}$ the reference plastic strain, σ_1 the maximum principal stress, σ_{th} the threshold stress, V_0 the representative volume element, σ_{ys} the current yield strength, $\sigma_{ys,0}$ the yield strength at calibration temperature and Σ denotes a unit stress. These were previously calibrated for an RPV steel in an unirradiated condition at a temperature T = -110°C [21]. The only value besides the yield strength that changes for this application is the temperature dependence of σ_u. Since the material was aged, the application scheme developed to handle irradiation embrittlement was not applicable; σ_u was therefore calibrated by tuning to simulated data. Since the measured T_0 is 20°C obtained with PCCV a/W = 0.5 specimens, data for the PCCV a/W = 0.5 were generated out of the Master Curve utilizing this reference temperature T_0. At the experimental test temperature T = 20 °C a data set was generated according to the previously explained scheme and rank ordered. The cumulative failure curve was then tuned to this data by varying the temperature shift ΔT in σ_u. The outcome is presented in Figure 14, with σ_u and σ_{min} values of 3847 and 1546 MPa respectively[4]. The obtained optimal temperature shift ΔT in σ_u due to the change in material, ageing and fit to

[4] The ORNL values for the σ_u and σ_{min} parameters are not available.

generated PCCV a/W=0.5 data is ΔT = 17 °C, which, together with (m, σ_{th}, $\varepsilon_{p,0}$, $\sigma_{ys,0}$), was then used for the prediction of the clad beams.

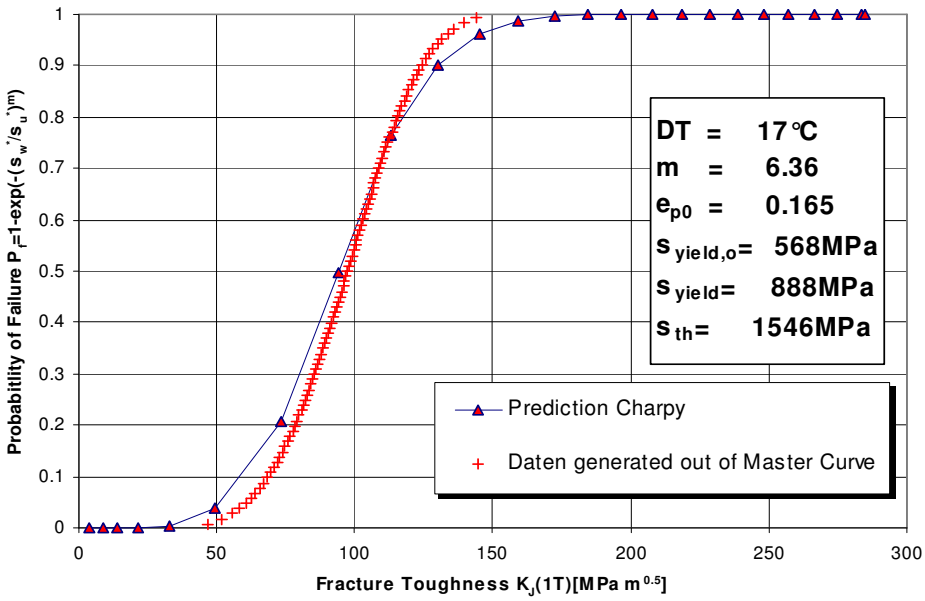

Figure 14 AREVA: Tuning the temperature shift: cumulative probability of failure vs. fracture toughness for PCCV a/W=0.5.

4.2.4 Inspecta

Inspecta performed finite element post-analyses of tests 1E4 and 1E7. The Master Curve methodology was used to determine fracture toughness of the base material. This gave T_o values of 19 and 22.8 °C for locations of respectively 18 mm and 3 mm below the interface.

Both 2D and 3D analyses were used to predict the fracture events in these two tests. Constraint parameters T-stress and Q were evaluated for both crack tips of each test. The finite element program ABAQUS was used for the analyses. The responses of Load –Line Displacement in the FEM analyses agreed very well with the test results. The crack driving forces and T-stress were calculated as a function of load for both tests. Constraint results of the tests indicated substantial loss of constraint at the shallow tips.

Prediction of fracture events of the tests by using the standard Master Curve methodology gave conservative results. Considering the constraint values at the crack tips and making correction to loss of constraint in the Master Curve methodology significantly improved the prediction of the fracture events in the tests.

4.2.5 Tractebel

The hereunder figures illustrate the 2D half-model (about 800 quadratic elements), the loading and the boundary conditions. A force is applied on 2 elements. The hinge (constraint) is located on one node. A non-linear analysis was performed with the assumption of plane strain conditions and small deformation. Even with a

relatively coarse 2D model in plane strain conditions, a correct residual stress field was obtained in the plane of the model by applying a thermal load (a temperature of 350°C). However, the perpendicular stress to the plane was unexpectedly very high. This influenced the J-calculation to such an extent that it was decided not to take the residual stress field into account. The contour dependence of the J-integral for such a thermal load appeared to be an additional difficulty.

Even with a 2D model, the agreement of the load line displacement was judged to be good. K_I was obtained on the basis of the J-integral calculation (G-θ method). K_{JC} values were calculated at the force F_i measured at experimental fracture. Estimations corresponding to displacement and energy at fracture were also calculated.

The value of T_0 at the crack tip at 3mm (T_0 = 22.8°C) was converted into K_{JC} following the Master Curve approach, taking into account the thickness correction of the specimen: K_{JC}(med) = 91 MPa√m; K_{JC}(5%) = 58 MPa√m; K_{JC}(95%) = 124 MPa√m. The probability of failure was also estimated based on the Master Curve method and its 3-parameter Weibull distribution.

4.2.6 IWM

IWM used a 3-D FE model to calculate crack driving force and constraint parameters; these were used in crack initiation and arrest analyses. The main conclusions are:

- Test 1E2 shows crack initiation at low fracture probability.
- Test 1E4 shows crack initiation at higher fracture probability.
- Initiation at lower crack tip is more probable due to smaller loss of constraint.
- Arrest in the cladding of test 1E2 can be explained from the J-integral of the arrested crack compared with the J-R curve.
- Break through of test 1E4 is not explained since from FE analysis, the crack arrest in the cladding would be expected, although at higher J values than for 1E2. Possible explanations include: a) higher real J due to dynamic magnification or b) lower J-R curve than reported.

4.2.7 VTT

The computation of crack initiation was performed for the “abnormal” specimen 1E7. One half of the actual crack shape was modelled. The Abaqus 6.7.1 [26] finite element code was used for the computation. The analyses were performed assuming thermo-elastic-plastic material behaviour and large strains and displacements. Mechanical loading was controlled by displacement that was applied in nodes of the loading line lying at a distance of 57 mm from the specimen transversal symmetry plane. Rigid support was modelled at a distance of 310 mm from the specimen transversal symmetry plane. Concerning residual stresses, the stress free temperature was taken as 350 °C, which leads to residual stresses due to difference in the thermal expansion coefficients of clad and base materials. The FE model with boundary conditions is shown in Figure 15. The stress-strain curves for aged base material were as defined in the problem definition documentation. For the cladding a lowered curve was utilised.

A boundary layer model was used to compute stresses corresponding to the small scale yielding reference state. These stresses were needed for evaluating the constraint parameter Q. The element mesh in the boundary layer model was defined for the circular domain of radius R (4000 mm) that contained a crack tip located at r = 0. The crack loading was determined by the J-integral computed by the domain integration technique in Abaqus. J-integral was computed as mean value from eight integration paths (3…10th path). T-stress was computed via the constraint parameter Q as:

$$Q = \frac{\sigma_\Theta(\bar{r}) - \sigma_\Theta^{SSY}(\bar{r})}{\sigma_0} = \frac{T}{\sigma_0} \quad , \tag{13}$$

in which σ_Θ and σ_Θ^{SSY} are the crack opening stresses from the component and the boundary layer (SSY) model corresponding to the same J level, and

$$\bar{r} = \frac{r}{J / \sigma_0} \quad , \tag{14}$$

in which r is radial distance from the crack tip and σ_o is yield stress.

Figure 16 presents the computed stress intensity factor along the crack front. The constraint (Q ≈ -1) and size corrected fracture toughness and the crack opening stress is also shown.

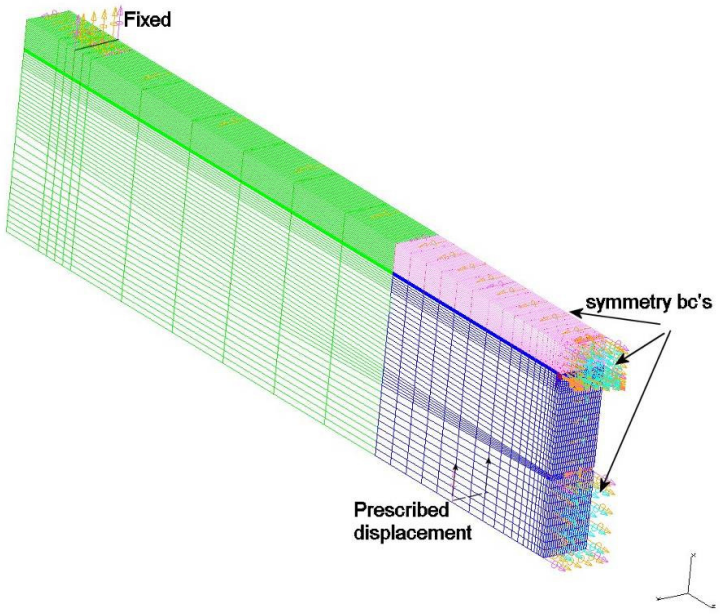

Figure 15 The VTT finite element model with boundary conditions.

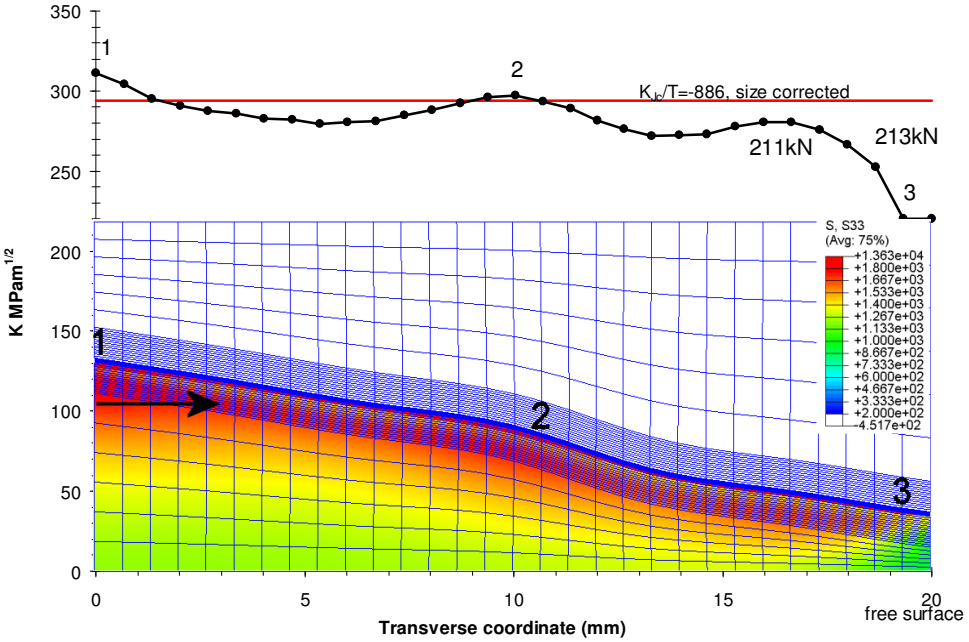

Figure 16 VTT computed stress intensity factor along the crack front. The constraint (Q ≈ -1) and size corrected fracture toughness and the crack opening stress is also shown.

4.2.8 Bay Zoltan Institute for Logistics

The aim of the work was to calculate the J-integral values for semi-large scale 4PB specimens, with different crack depths. Three specimen geometries were analyzed: 1E2, 1E4 - short crack, both crack tips are sharp, 1E7 – long crack, one crack tip is sharp, the other one is drilled out. The analysis was performed in two cases: straight crack front, and real crack front:

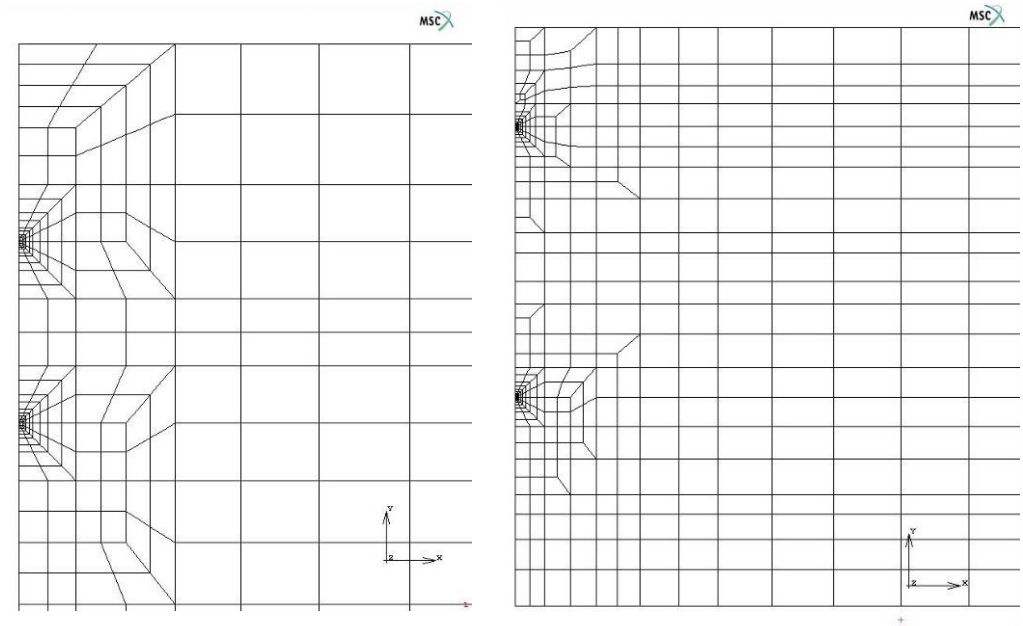

a) Specimen with short crack (1E2 and 1E4)

b) Specimen with longer crack (1E7)

Figure 17 Crack tip meshes used by BZLOGI.

MSC MARC 2005r3 code was used for the model generation and calculation. 20 nodes hexahedron elements were applied for the structural discretization. In case of straight crack front only one quarter of specimen was modelled due to the symmetry properties, but in case of real crack front half the specimen had to be modelled. The residual stress was also taken into account. The stress free temperature method was applied to determine the residual stress, with the stress free temperature: T=350°C. The thermal expansion coefficients were also given by NRI. In the first few seconds of the analysis time the mechanical load was zero, and the temperature decreased from the stress free temperature to room temperature. After this the mechanical load started to increase up to the total load, and the temperature was held constant.

J-integral values were calculated for all crack tips of specimens at different integration paths. At certain crack tips more integration radii were defined, and that result was taken, where the J-integral values reached a constant value. J-integral values were post-processed along the crack front of all specimens. Of course, both cases were plotted: for straight and real crack front. In cases of short cracks the difference was not so significant between the results, but in case of long crack, the real crack front geometry gives a better result. The J-integral values versus time curves were plotted at side and centre nodes of the crack front in all cases.

In this study, three specimens were analyzed, and 3D finite element model was generated for each of them. J-integral was calculated for each of the sharp crack tips. Straight crack fronts were modelled to simplify the analysis, and average crack depths were considered. Residual stresses were taken into account in the calculation.

The effects of moving the crack fronts (simulation of pop-ins) were analyzed separately: only one crack front was moved in two cases, and both crack fronts were moved at the same time. Elastic-plastic material properties were applied, and the residual stresses were considered in the analysis. J-integral values were plotted along the crack fronts for all cases. dJ/da diagrams were also generated to show the effect of increased crack size on the J-integral values. A summary about the relative variation of J-integral is also given. The main conclusions were:

- If the upper crack tip is moved up (simulating crack growth towards the clad), the J-integral value is increased at the upper and at the lower crack tip.
- If the lower crack tip is moved down (simulating crack growth into the bulk of the specimen), the J-integral value is increased only at the upper tip, while that at the lower crack is approximately unchanged.
- If both crack tips are moved (simulating growth in both directions) the J value is increased at both crack tips.

4.3 Intercomparison of the FE Predictions

Basic information about the FE calculations performed by the individual partners is summarised in Table 9.

Table 9 Summary of the FE models.

Organisation	Model	Code	Crack Front	Type of calculation	Specimens evaluated
AREVA NP	3D	ABAQUS	straight	elastic-plastic	1E2
BZLOGI	3D	MSC.MARC	straight, real	elastic-plastic	1E2, 1E4, 1E7
INSPECTA	2D, 3D	ABAQUS	straight	elastic, elastic-plastic	1E4, 1E7
IWM	2D	ABAQUS	straight	elastic-plastic	1E2, 1E4
ORNL	3D	ABAQUS	straight	elastic, elastic-plastic	1E2, 1E4, 1E7
TRACTEBEL	2D	SYSTUS	straight	elastic-plastic	1E2, 1E4, 1E7
VTT	3D	ABAQUS	real	elastic-plastic	1E7
NRI	3D	SYSTUS	real	elastic, elastic-plastic	1E2, 1E4, 1E7

4.3.1 Force vs. LLD (CMOD) behaviour

Figure 18, Figure 19 and Figure 20 compare the calculated force vs. LLD predictions from individual partners with the test data for specimens 1E2, 1E4 and 1E7 respectively. In general there is good agreement (even for the 2D calculation). However in the case of the force vs. CMOD curve for abnormal specimen 1E7 (Figure 21) the 2D calculation overestimates the force values in the later stages of the test. It should be noted that some of the 3D calculations also somewhat overestimated the force, in particular those of BZLOGI and NRI. NRI solved this problem by decreasing values of input stress-strain curves by 10%.

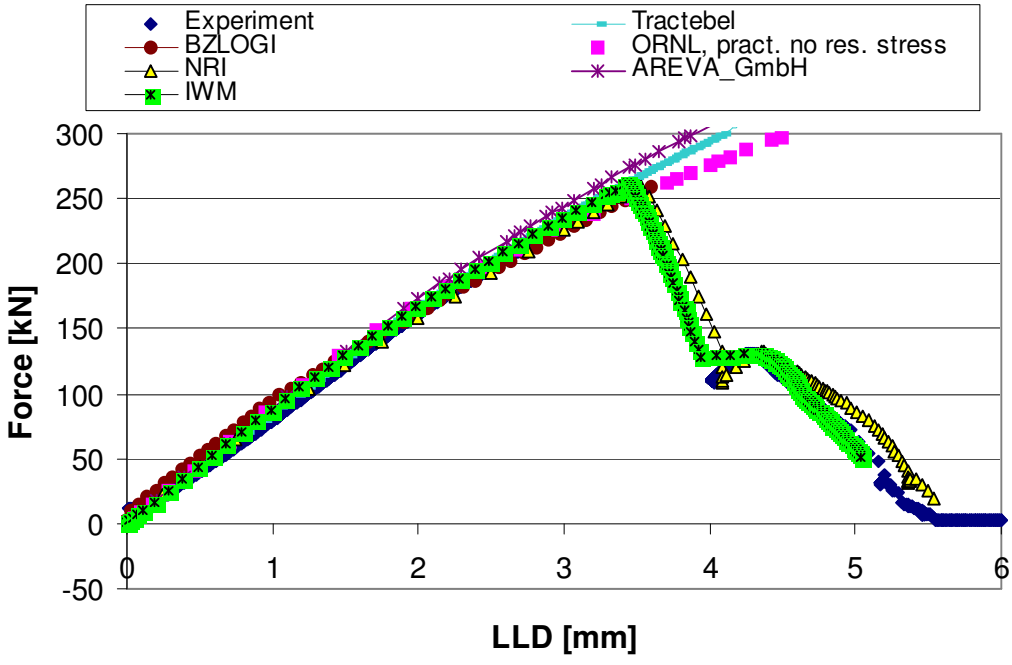

Figure 18 Comparison of predicted load – displacement behaviour for specimen type 1E2 (normal crack height, pop-in fracture).

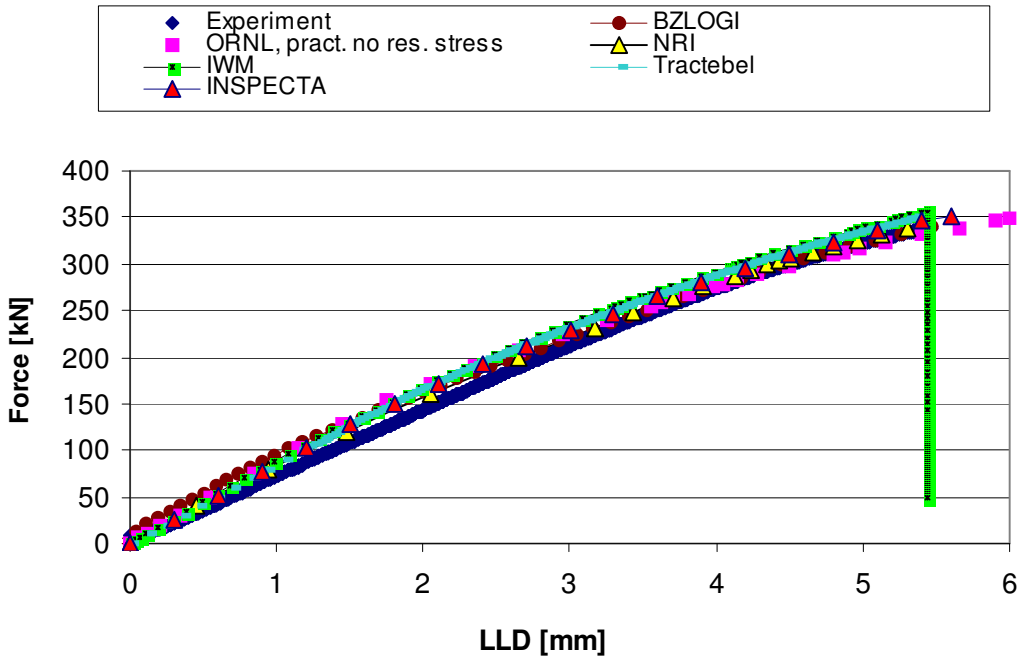

Figure 19 Comparison of predicted load – displacement behaviour for specimen type 1E4 (normal crack height, immediate fracture).

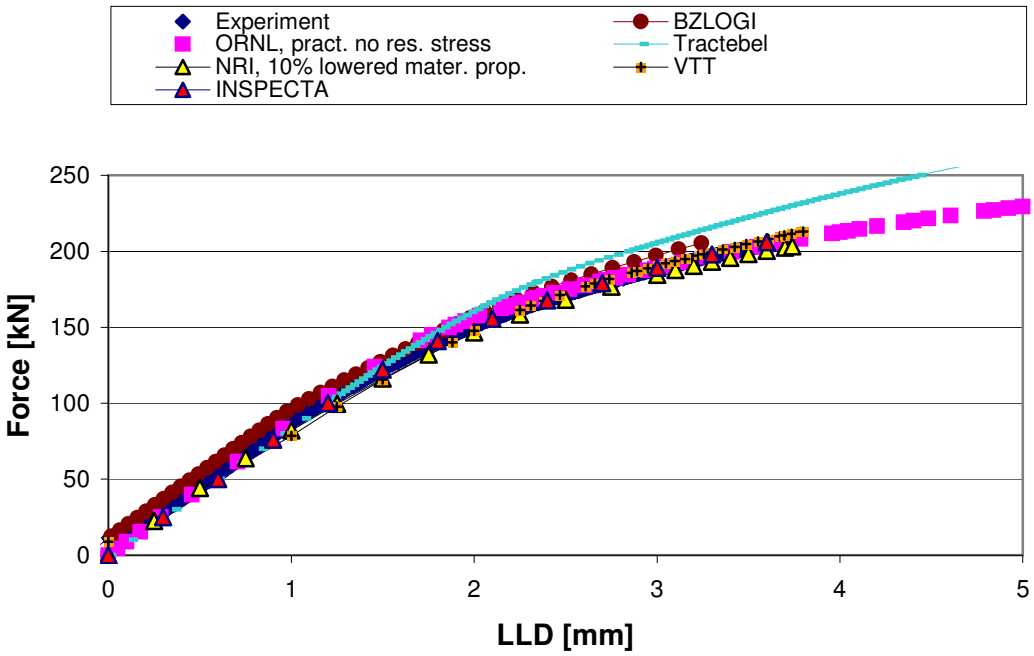

Figure 20 Comparison of predicted load – displacement behaviour for specimen type 1E7 (long "abnormal" crack height, pop-in fracture).

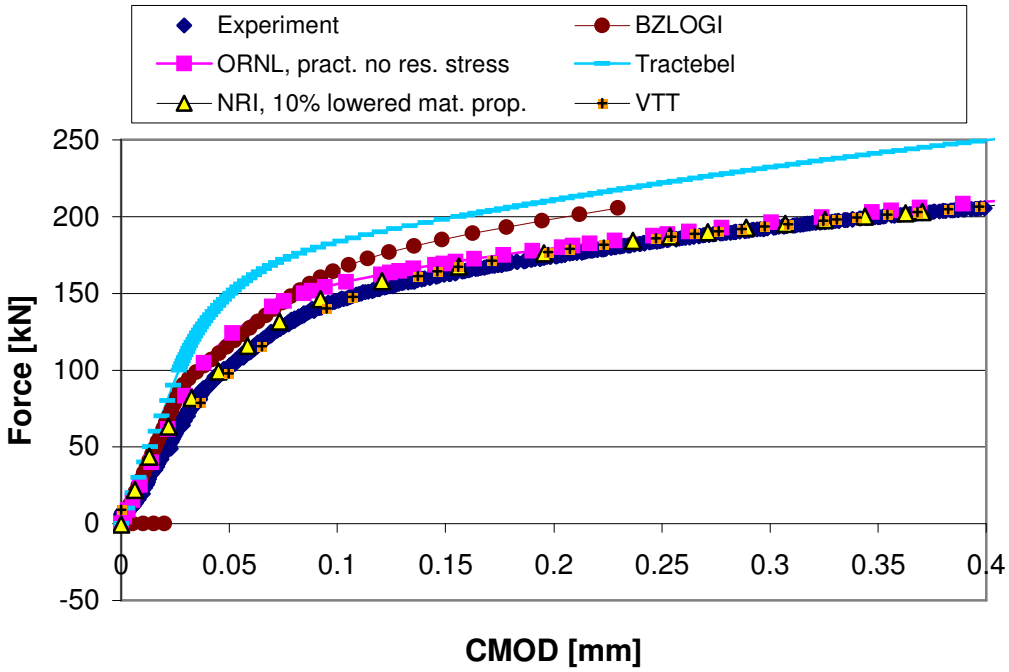

Figure 21 Comparison of predicted load – CMOD behaviour for specimen type 1E7 (long "abnormal" crack height, pop-in fracture).

4.3.2 K_J vs. Load

Figure 22, Figure 23, Figure 24, Figure 25 and Figure 26 show the development of the elastic-plastic stress intensity factor K_J with loading. ORNL, Areva GmbH, Inspecta and Tractebel chose not to model residual stress, and their K_J-values start from zero for zero applied bending load. In contrast the BZLOGI, IWM and NRI analyses included residual stresses, and as a result their K_J-values are non-zero at zero bending load. The only difference between these is that NRI assigned artificially negative values of K_J to those load levels for which the residual stress dominates above the bending load i.e. closing of crack due to residual stresses prevails over opening the crack by bending loading.

From Figure 22 and Figure 23 (for specimen 1E2) good accordance is seen between the K_J-values from the BZLOGI, IWM and NRI calculations. On the other side, in these figures not too good accordance in K_J-values development was shown for calculations in which residual stresses were not taken into account (ORNL, Areva, Tractebel). In case of Tractebel, this may be due to the use of a 2D model.

In Figure 24 and Figure 25 (for specimen 1E4), relatively good agreement was obtained between the ORNL and Inspecta K_J results; both used ABAQUS and residual stresses not taken into account. The BZLOGI and NRI analyses (MARC and SYSTUS respectively, both took residual stress into account) showed very good agreement, but IWM solution showed significant deviation with lower K_J values. The reason for this is not clear, but it may be due to the 2D model used by IWM (this finding would be consistent with the result of the other 2D calculation, by Tractebel, which also shows lower values of K_J values compared to those of

the 3D calculations). The good agreement of the IWM 2D solution for specimen 1E2 with the 3D solutions of BZLOGI and NRI would appear incidental.

Comparison of K_J values in the case of specimen 1E7 (Figure 26) is hampered by the fact that NRI and VTT artificially decreased the stress-strain properties by 10%, and in consequence obtained higher values than would otherwise have been the case.

Table 10 details the values of K_J at the fracture initiation load for all three specimens. The differences between the reported values correspond to the factors discussed above.

Table 10 Values of K_J the load at which fracture initiation occurred.

	INSPECTA	BZLOGI	ORNL	TRACTEBEL	AREVA GmbH	IWM	VTT	NRI
1E7, Average K, shallow	347	203.5	324.7	210.5	-	-	286.3	273.0 *)
1E2, Average K, deep	-	77.5	105.5	69.7	93.1	76.4	-	75.0
1E2, Average K, shallow	-	116.2	160.3	102.5	139.4	115.8	-	111.5
1E4, Average K, deep	230	172.2	196.7	157.1	-	153.2	-	167.5
1E4, Average K, shallow	302	233.7	271.5	230.5	-	210.4	-	235.5

*) 10% lowered mat. prop.; green colour = good accordance, red colour = increased values due to not modelling res. stresses, brown colour <=> 2D values (either a little lower values, or good accordance)

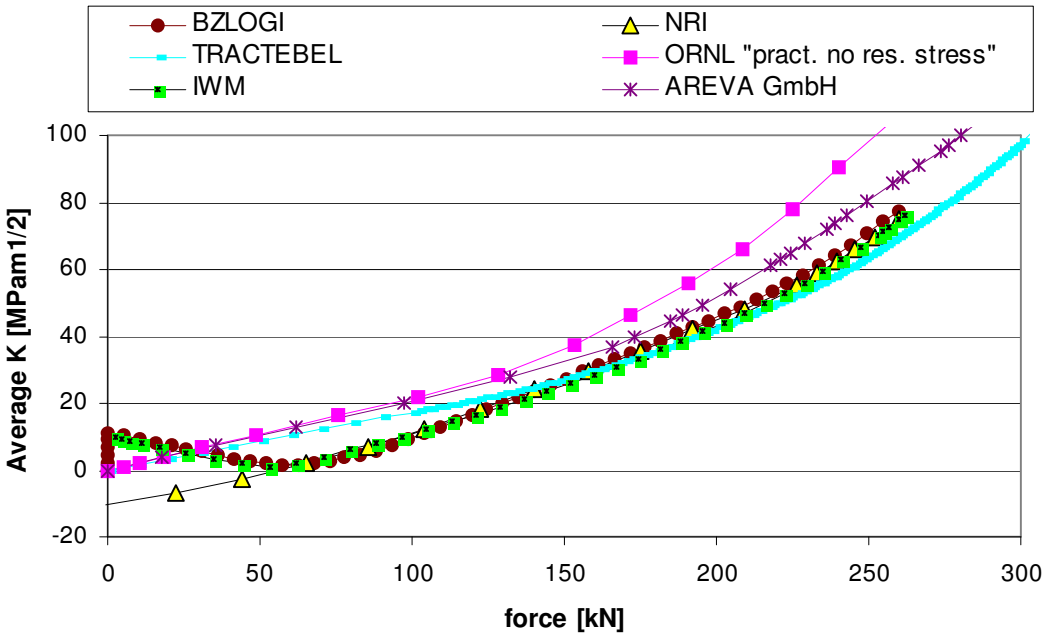

Figure 22 Comparison of predicted average crack driving force along the lower crack front as function of applied load for specimen type 1E2 (normal crack height).

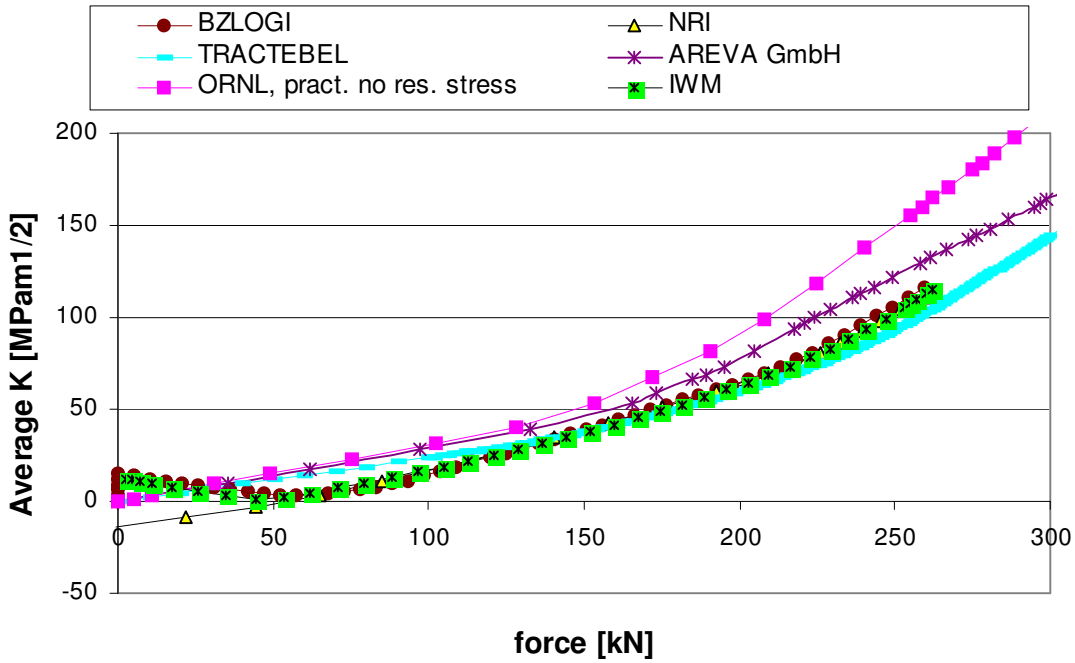

Figure 23 Comparison of predicted average crack driving force along the upper crack front as function of applied load for specimen type 1E2 (normal crack height).

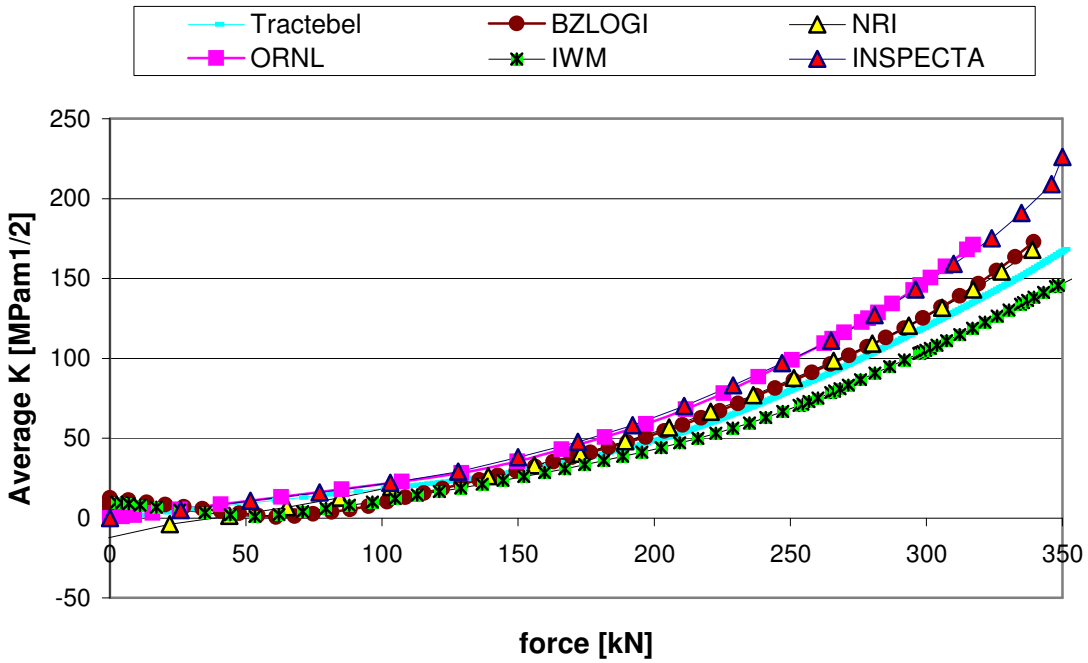

Figure 24 Comparison of predicted average crack driving force along the lower crack front as function of applied load for specimen type 1E4 (normal crack height).

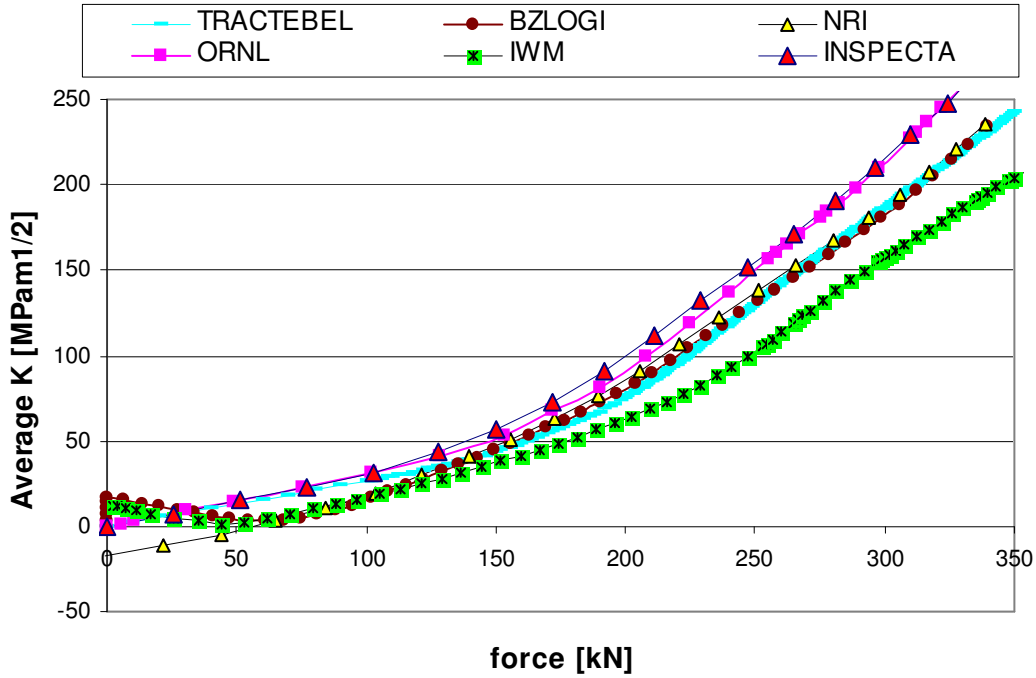

Figure 25 Comparison of predicted average crack driving force along the upper crack front as function of applied load for specimen type 1E4 (normal crack height).

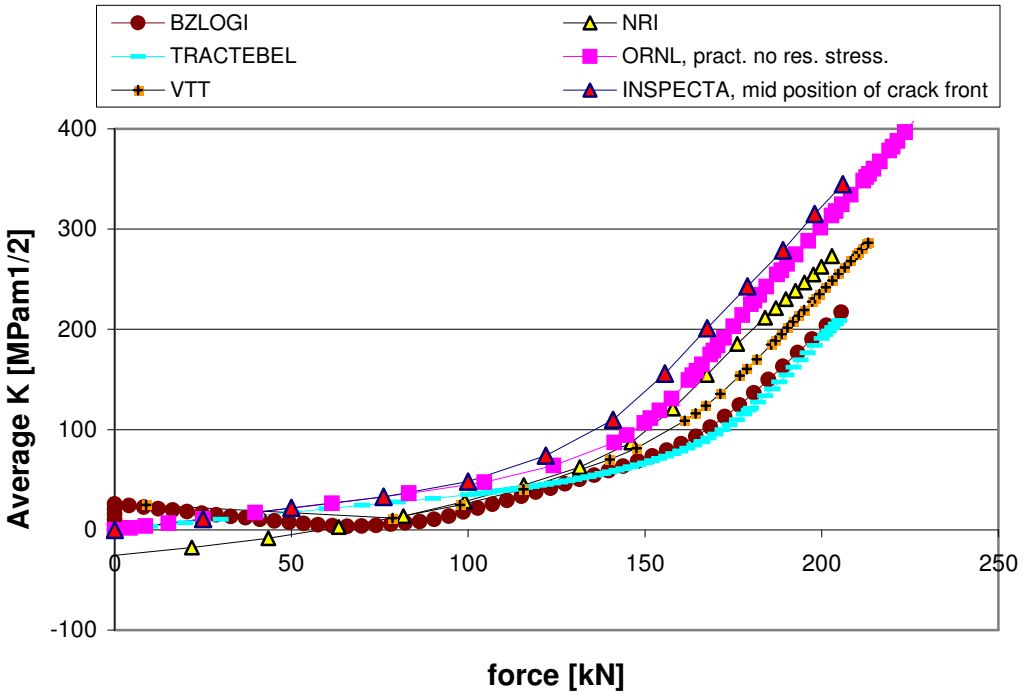

Figure 26 Comparison of predicted average crack driving force along the upper crack front as function of applied load for specimen type 1E7 (long "abnormal" crack height).

4.3.3 Variation of K_J along crack front

Comparisons of the predicted variation of K_J along the crack fronts are shown in Figure 27, Figure 28, Figure 29, Figure 30 and Figure 31. A decrease in J near the flank (free surface) is evident. In some cases there are indications about small increase about 5 mm below the flank surface, but this is a minor effect compared to the decrease of J towards the free surface.

As to be expected the J variation depends on whether the FE mesh modelled the actual crack front profile after fatigue sharpening or assumes a straight crack front. In the case of the latter, the J values are fairly constant in the middle part of the specimen. When the waviness of the real pre-fatigued crack front is modelled, the J-integral shows a moderate corresponding variation. In Figure 31 (upper crack front of 1E4) the J values from VTT show two apparent inconsistencies with respect to the NRI predictions: first, the increase of J in the mid-point of crack front is not considered realistic and has probably arisen by modelling one half of a crack front which in reality was not perfectly symmetric, but then implicitly assuming symmetry in the FE model; secondly, the J-profile shown corresponds to an applied force of 213 kN, which is a little higher than the value at cleavage fracture initiation (205 kN).

The BZLOGI analyses included a direct comparison between a modelling real and straight crack fronts, as may be seen from Figure 32a-c. It is seen that some effect on J exists, but at the lower tip which experienced lower J values (generally below150 kJ/m^2) this is almost small enough to be neglected. For the upper tip with higher loads the difference appears significant. Overall the trend is that real crack front profiles give lower J values.

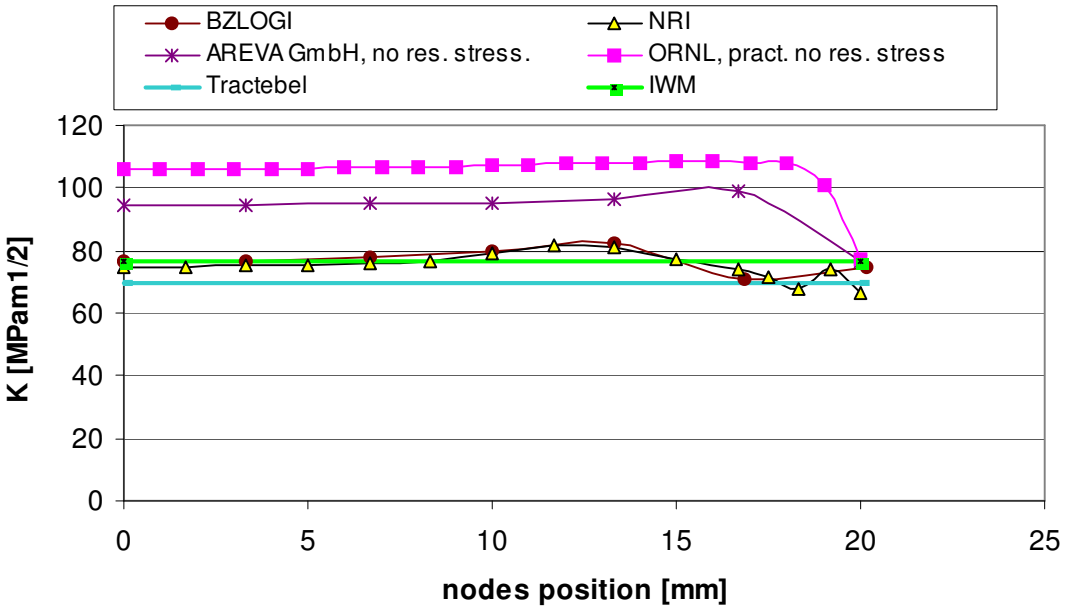

Figure 27 Comparison of predicted crack driving force along the lower crack front for specimen type 1E2 (normal crack height) at the fracture/pop-in load.

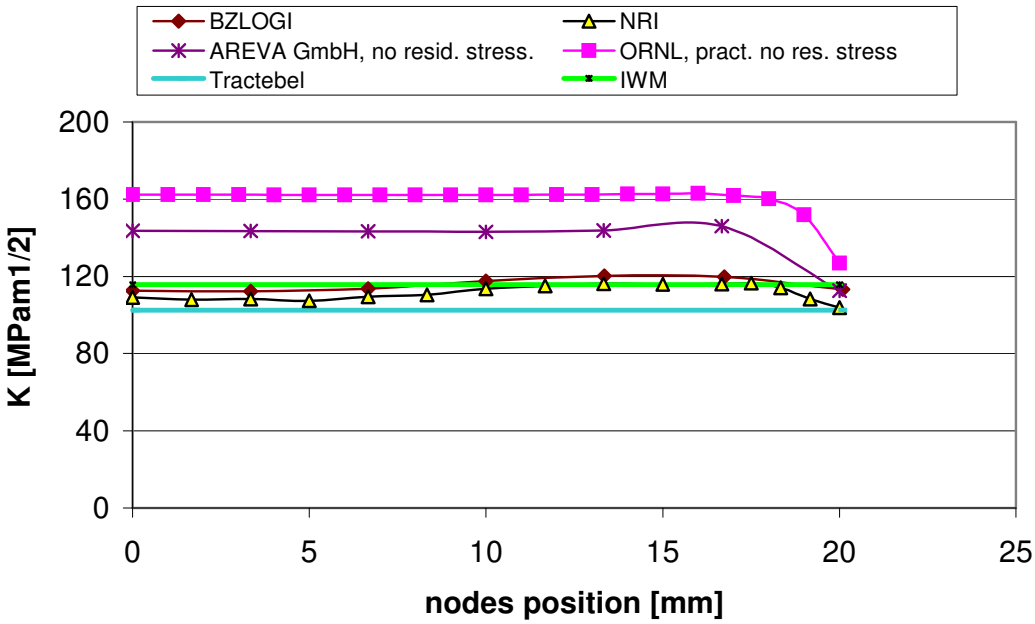

Figure 28 Comparison of predicted crack driving force along the lower crack front for specimen type 1E2 (normal crack height) at the fracture/pop-in load.

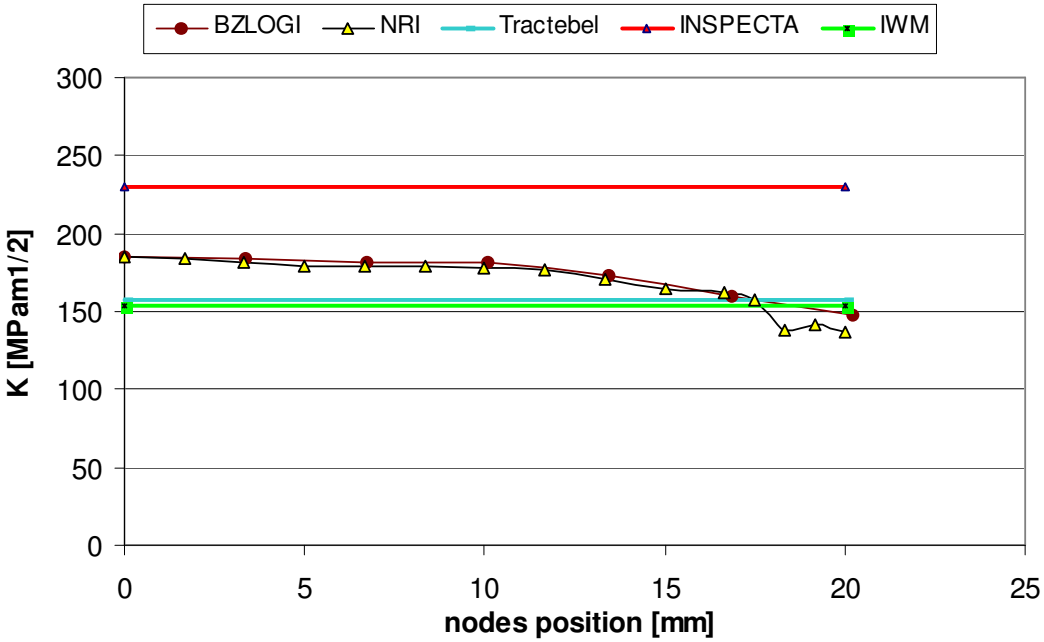

Figure 29 Comparison of predicted crack driving force along the lower crack front for specimen type 1E4 (normal crack height) at the fracture/pop-in load.

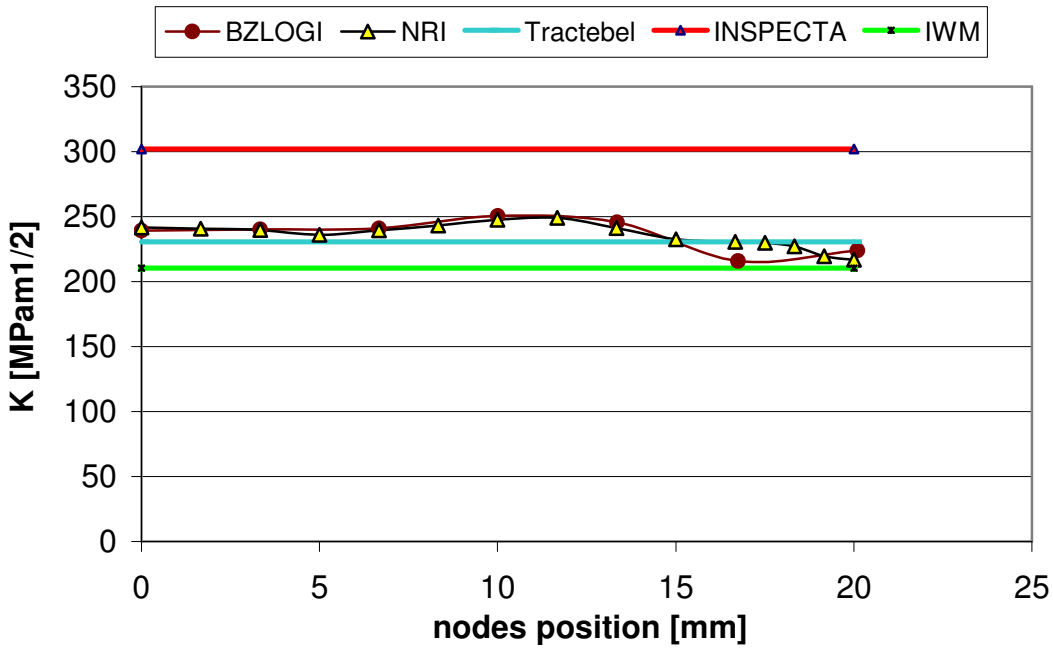

Figure 30 Comparison of predicted crack driving force along the upper crack front for specimen type 1E4 (normal crack height) at the fracture/pop-in load.

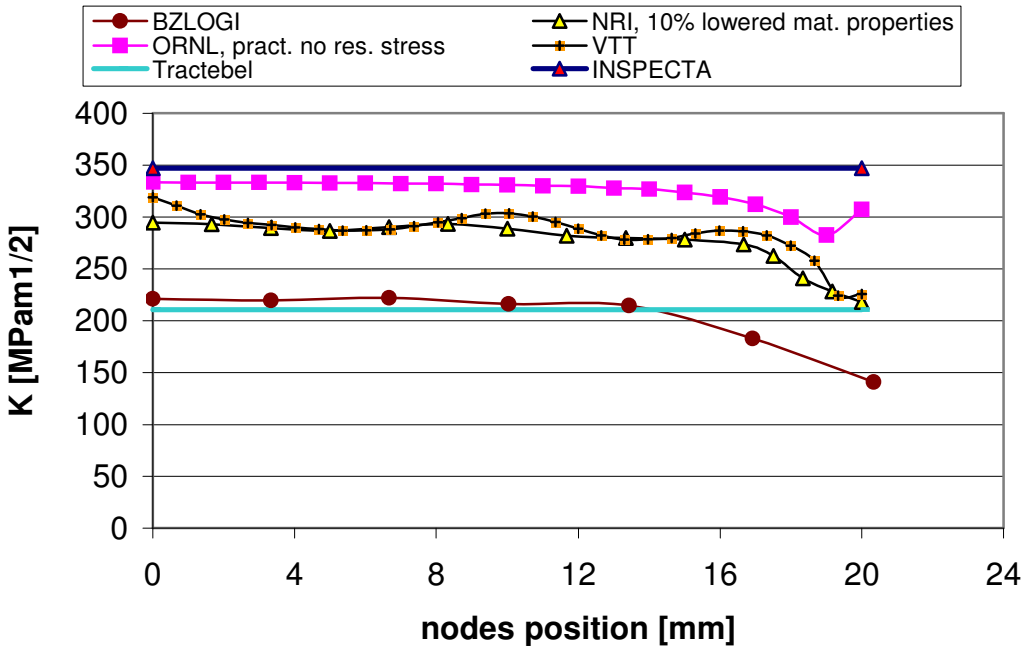

Figure 31 Comparison of predicted crack driving force along the upper crack front for specimen type 1E7 (normal crack height) at the fracture/pop-in load.

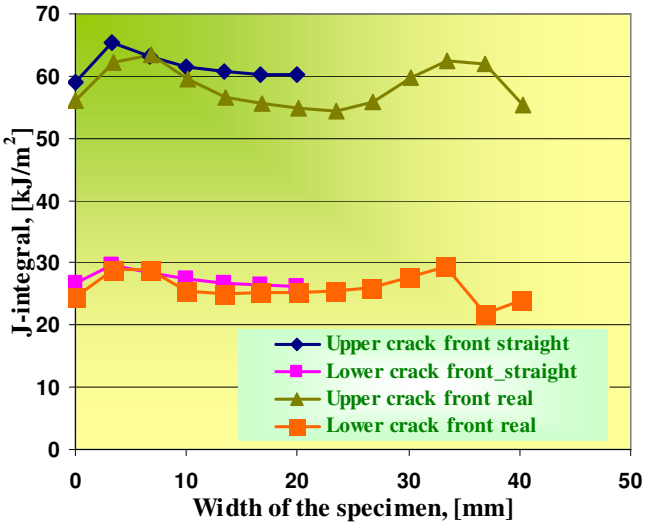

a) 1E2

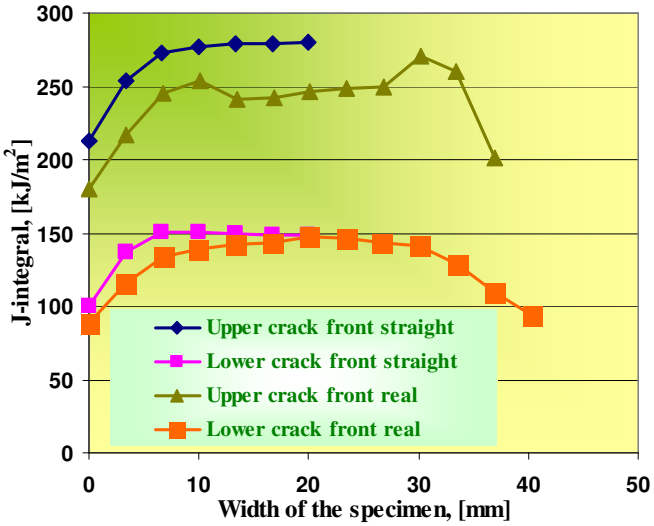

b) 1E4

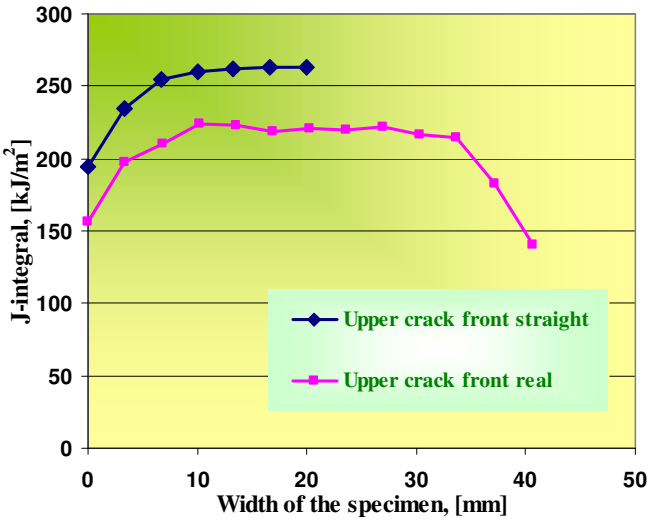

c) 1E7

Figure 32 Predicted J values along the crack front for the different specimens at the fracture/pop-in load.

4.3.4 Weibull stress

Figure 33 shows examples of the Weibull stress trajectories for deep and shallow cracks from the ORNL local approach analysis. Equivalent data were not reported by AREVA and hence no comparison is made.

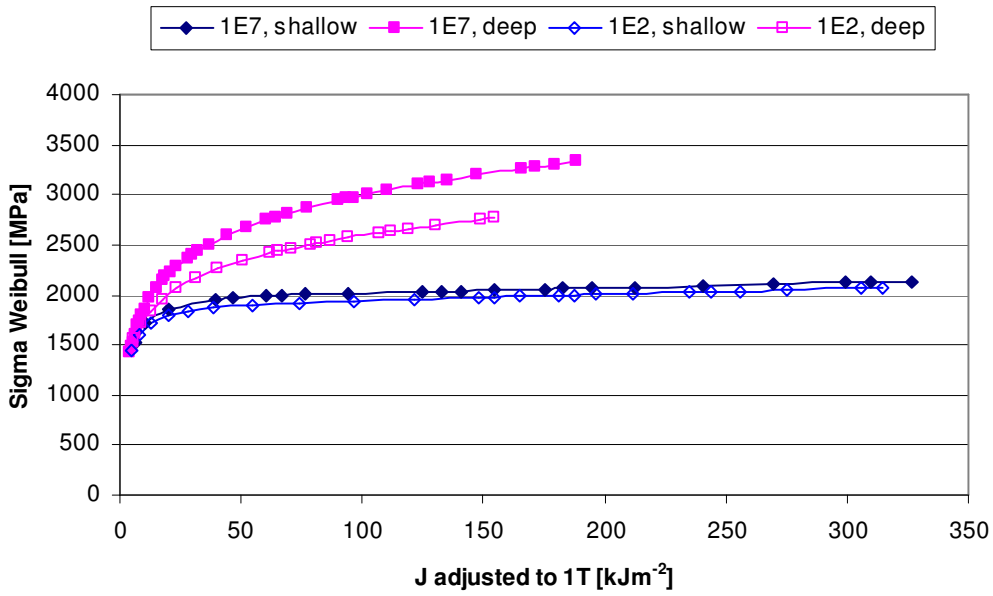

Figure 33 ORNL predictions of Weibull stress as function of J.

4.3.5 Constraint parameters

Several of the participating organisations calculated constraint parameters such as elastic T-stress, elastic-plastic T-stress, Q and Q_H parameters as functions of applied load (Table 11)

Table 11 Methods used to consider loss-of constraint effects.

Analysis	Constraint Parameter
INSPECTA	Elastic T, Q
BZLOGI	-
ORNL	Elastic T, Q_H
TRACTEBEL	-
AREVA NP GmbH	-
IWM	Elastic T, Elastic-Plastic T
VTT	Elastic T, Q
NRI	Elastic T, Elastic-Plastic T, Q

Table 12 summarises the numerical values at the load corresponding to cleavage initiation for each of the three specimens; for convenience, the Q and Q_H parameters are multiplied by the yield stress to allow them to be expressed in MPa and thus more easily included in plots with the T-stress values. Figure 34 (1E2, shallow tip),

Figure 35 (1E2 deep tip), Figure 36 (1E4 shallow tip), Figure 37 (1E4 deep tip) and Figure 38 (1E7 shallow tip) provide a graphical comparison of the values obtained by different analysts.

Table 12 Predicted constraint parameter values (MPa) at the fracture load.

Specimen,crack tip,constraint parameter	NRI	NRI w/o σ_R	ORNL	VTT	INS-PECTA	IWM (2D)
1E2,upper, elastic T	-433	-472	-602	-	-	-520
1E2,upper, el-pl T	-578		-	-	-	-
1E2,upper, $Q^*\sigma_y$	-1095		-1197	-	-	-914
1E2,lower, elastic T	-227	-235	-280	-	-	-230
1E2,lower, el-pl. T	-65		-	-	-	-
1E2,lower, $Q^*\sigma_y$	-458		-346	-	-	-284
1E4,upper, elastic T	-626	-676	-786	-	-795	-
1E4,upper, el-pl. T	-975		-	-	-	< -1000
1E4,upper, $Q^*\sigma_y$	-1121		-	-	-1154	-1126
1E4,lower, elastic T	-352	-375	-368	-	-370	-
1E4,lower, el-pl. T	-65		-	-	-	< -200
1E4,lower, $Q^*\sigma_y$	-375		-	-	-311	-346
1E7, upper, elastic T	-372	-496	-558	-	-570	-
1E7, upper, el-pl. T	-1156		-	-887	-	-
1E7, upper, $Q^*\sigma_y$	-		-	-	-1110	-

The results for all three specimens indicated that constraint loss occurs at both tips (negative T-stress and $Q.\sigma_y$ values), but as expected this is significantly larger at the upper (shallow) crack tip compared to the lower (deep). Quantitatively the numerical values for individual parameters differ between the various analyses, indicating sensitivity to modelling assumptions (residual stress, mesh effects etc) and calculation methods. Overall the main features are:

(1) For elastic T-stress, ORNL and Inspecta obtained approximately similar values for specimens 1E4 and 1E7. The corresponding NRI results (without residual stresses) are not far from their values. N.B. NRI calculated the elastic T-stress for 1E2 both with and without the initial residual stresses to better understand the effect on the results.

(2) The Q values obtained by partners NRI, Inspecta, and IWM for specimen 1E4 were in reasonable agreement. Residual stresses (in this particular case) increase a little constraint at both lower and upper crack fronts (as expected).

(3) In general, no extremely large discrepancy between values provided by individual partners for the same type of constraint parameter, was found. For elastic-plastic T-stress the results to be compared are scarce.

It should be noted that values of elastic T-stress were determined via value of applied (experimental) force at fracture initiation. For the beam tests under consideration here, significant plasticity effects were present and the elastic stress distributions do not reflect the actual stress state at the crack tip. In fact, determination of elastic T-stress for an "elastic-plastic experiment" means determination of slope in curve T-stress vs. load (or T-stress vs. displacement), without determining the moment of fracture. The accordance in the slopes between different partners may be then considered as accordance in determination of T-stress. In case that for some reasons (such as the need to provide its value in MPa, etc.) the value of T-stress is required, then moment of fracture should be determined based on force.

Finally, it is seen that the elastic-plastic T-stress distinguishes in a more pronounced way between the two constraint states at lower and upper crack fronts than does the elastic T-stress i.e. the values are higher at the upper tip and lower at the deep tip. Use of the elastic-plastic T-stress as a constraint parameter is further substantiated by two additional factors:

(1) For a two-parameter constraint loss approach using K_J, using a quantity of elastic-plastic nature is more consistent with the calculation of J (and with the physical behaviour).

(2) Conventionally the Q parameter has been preferred in the elastic-plastic range; however an advantage of using elastic-plastic T-stress is that its determination is significantly easier and a coarser mesh may be used.

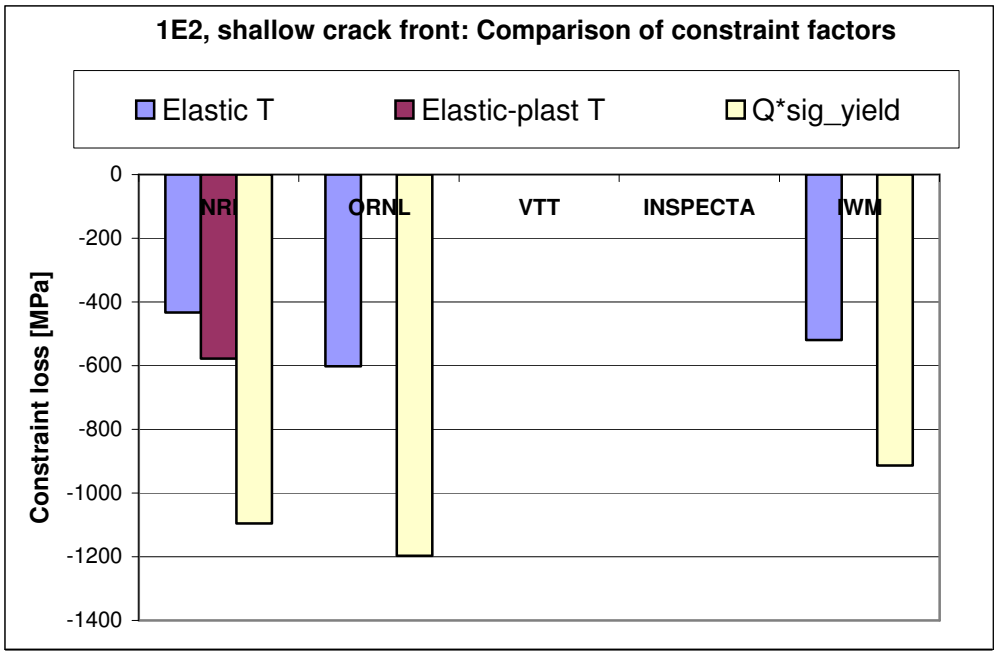

Figure 34 Comparison of predicted constraint loss for the shallow crack front on specimen 1E2 in terms of the elastic T, elastic-plastic T and Q parameters.

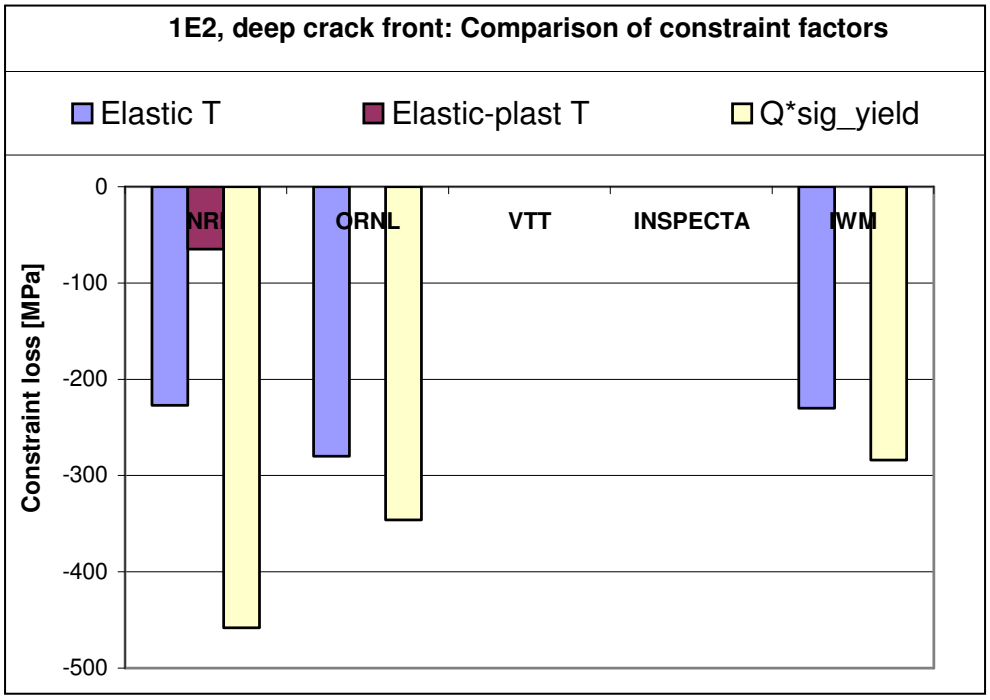

Figure 35 Comparison of predicted constraint loss for the deep crack front on specimen 1E2 in terms of the elastic T, elastic-plastic T and Q parameters.

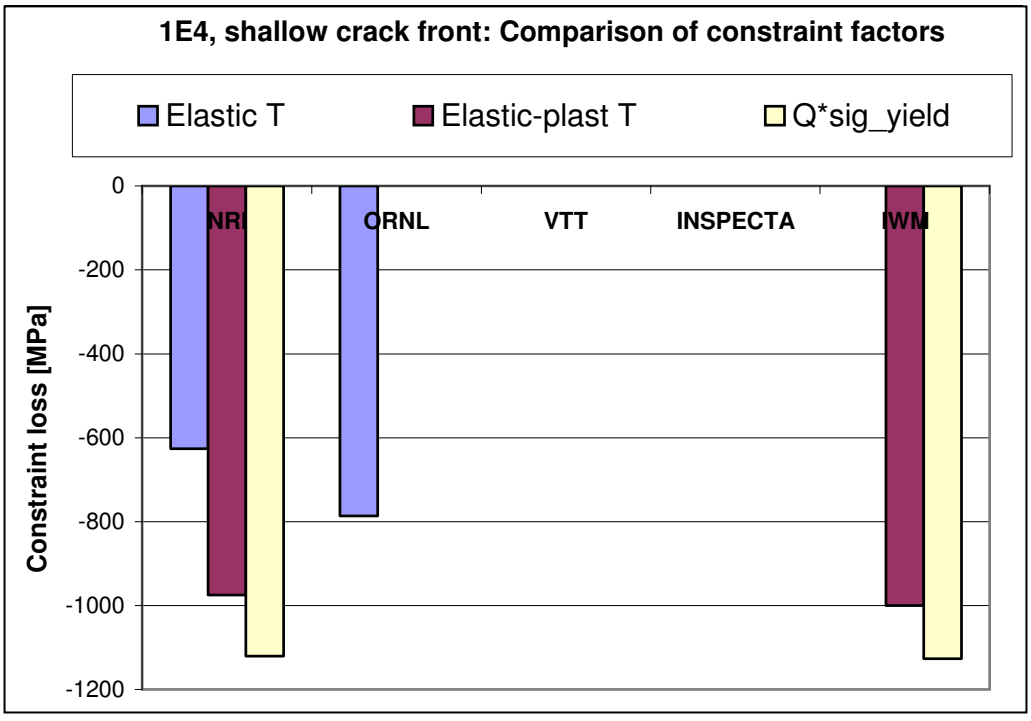

Figure 36 Comparison of predicted constraint loss for the shallow crack front on specimen 1E4 in terms of the elastic T, elastic-plastic T and Q parameters.

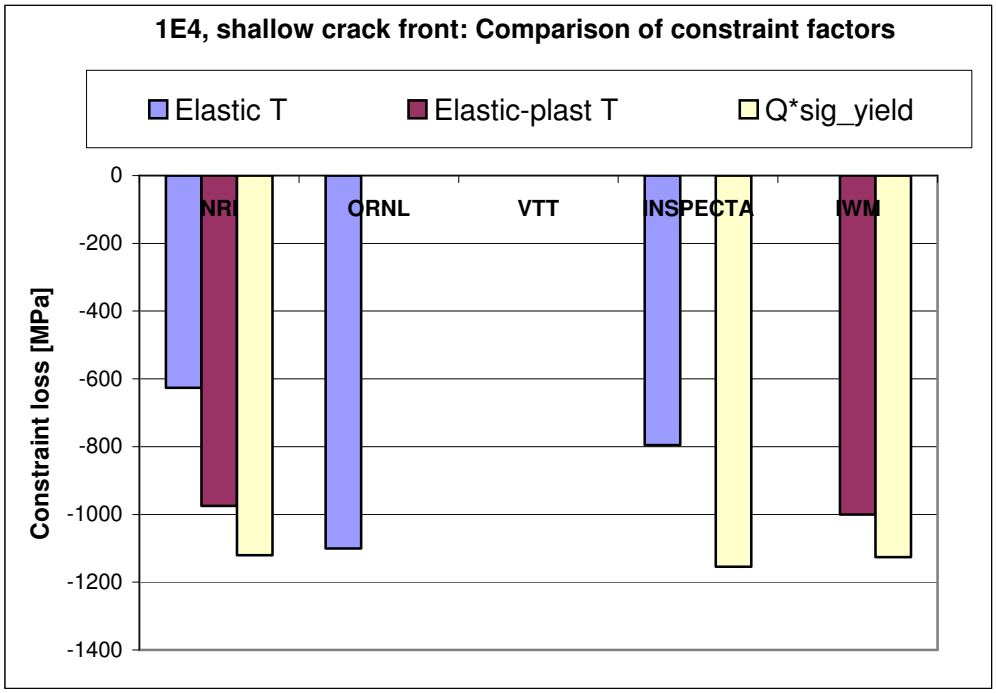

Figure 37 Comparison of predicted constraint loss for the deep crack front on specimen 1E4 in terms of the elastic T, elastic-plastic T and Q parameters.

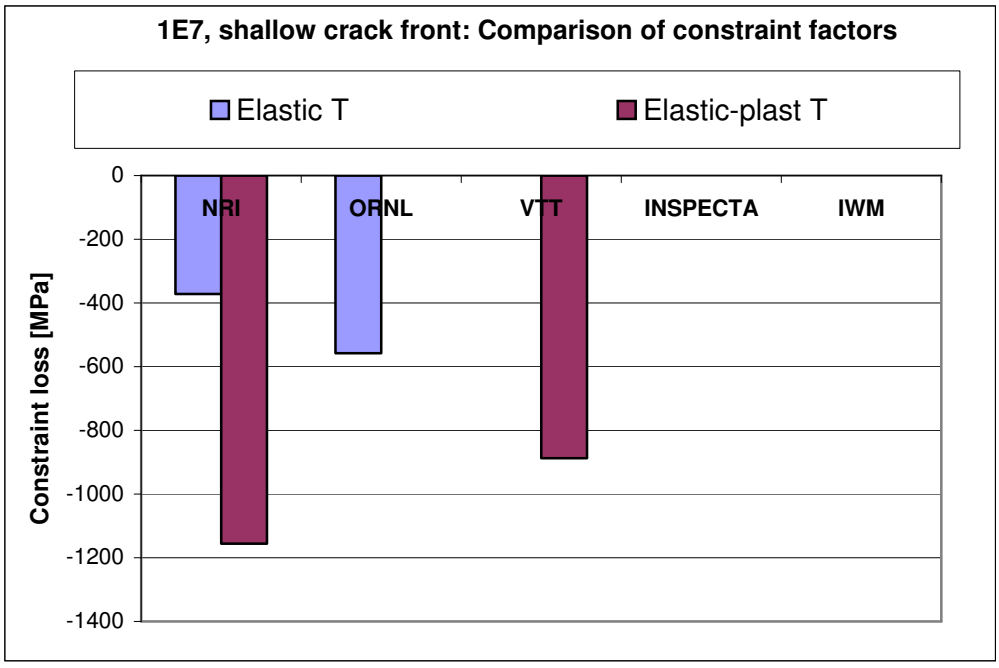

Figure 38 Comparison of predicted constraint loss for the shallow crack front on specimen 1E7 in terms of the elastic T, elastic-plastic T and Q parameters.

5 DISCUSSION

5.1 Sensitivity of K_J to Modelling Assumptions

The FE analyses have allowed the effect of several modelling parameters to be assessed. The results can be summarised as follows:

- For the beam geometry and material properties considered, 2D models were found to produce lower values of K_J compared to 3D models. This implies that using a 2D model for such cases may be non-conservative.
- Modelling real crack front geometry after pre-cracking is more accurate than modelling straight crack front, but since the model with straight crack fronts produced higher values of J, it may be used as a conservative approximation of a model with real crack front.
- Incorporating the residual stresses due to the clad has also significant effect on J-values, so it is advisable to include them into the FE analysis. In the examined configuration (material properties, geometry of crack, loading conditions, etc.), omitting residual stresses in the model produced higher values of J compared to the case when they are modelled, and consequently, this approach was conservative.

5.2 K-Based Approaches for Predicting Fracture Initiation

5.2.1 Master Curve Assessment

The most straightforward approach to assessing the likelihood of fracture initiation is to compare the crack tip driving force with the value of fracture toughness for the material at the test temperature. Since the material fracture properties were evaluated using the master curve methodology, this has provided the baseline for the present case. Since the test temperature effectively corresponded to the T_0 value, the Master Curve predicted K values for fracture probabilities of 5, 50 and 95% are 62, 100 and 136 MPa$\sqrt{m}$ respectively. On this basis Figure 39 and Figure 40 compare the K_J values obtained from the FE evaluations of the experiments with these master curve material fracture toughness predictions for the shallow and deep tips respectively.

Since only a limited number of specimens were considered in the project no statistically valid conclusions can be drawn. However the results are consistent with the hypothesis that such an application of the master curve to assess cleavage initiation at the upper tip would lead to conservative predictions i.e. at loads below those for which pop-in or fracture occurred in the test themselves. This is attributed to a substantial constraint loss effect at the upper tip, as discussed in the following sections.

On the other hand, the K_J values for the lower tip obtained from FE evaluations of experiment fall within the predicted range of master curve fracture toughness.

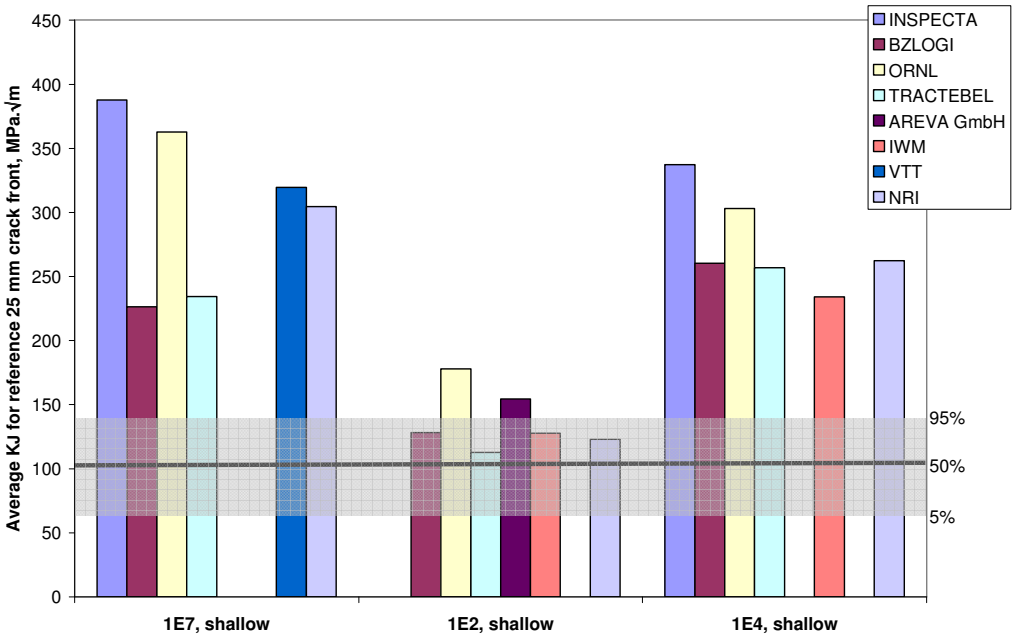

Figure 39 Comparison of the predicted crack driving force values at the upper (shallow) tip for the load at which fracture or pop-in occurred, with the range predicted by the fracture toughness master curve for the material at the test temperature.

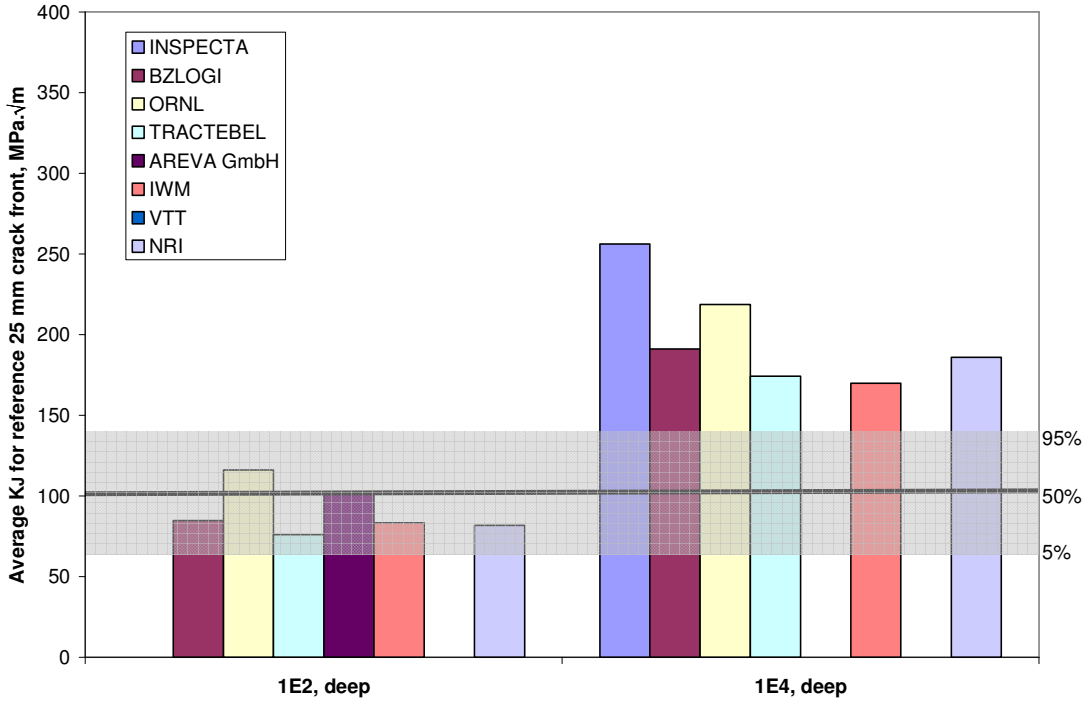

Figure 40 Comparison of the predicted crack driving force values at the lower (deep) tip for the load at which fracture or pop-in occurred, with the range predicted by the fracture toughness master curve for the material at the test temperature.

5.2.2 Failure Assessment Diagram Methods

British Energy investigated the application of the R6 FAD methodology [1] to the tests. The analysis uses simple beam theory to estimate stresses in a composite beam, with SIF solutions from the R-code (this approach had produced crack driving forces that agreed well with 2D cracked body analyses for NESC-IV). A global reference stress solution was derived for a composite beam (plane stress & plane strain). R6 does prescribe a fracture toughness transition curve as such, however methods such as the Master Curve are typically used to provide estimates of K_{mat} if appropriate experimental data is not available for the relevant temperature range and material condition. Here predictions of expected behaviour were based on the master curve P_f = 50% value of the fracture toughness to calculate K_r. Figure 41 shows the FAD (plane stress analysis), from which it appears that 1E4 and 1E7 failed at the collapse cut-off and that constraint effects appear to be active at the upper tips of 1E4 and 1E7. On the other hand, 1E2 has failed below the mean. It should be noted however that all the remaining PHARE tests would need to be added to get statistical significance.

The analysis also considered the procedure in R6 Section III.7 to reduce potential over-conservatism by taking into account of constraint loss effects. For this the FAD curve can be modified via the relation:

$$K_r = f(L_r)\left[1 + \alpha\left(-\beta L_r\right)^m\right] \qquad (15)$$

Where the β parameter is defined either in terms of the T-stress or Q, while α and m are derived[5] from fracture toughness test data at different constraint levels using the relationship:

$$K^c_{mat} = K_{mat}\left[1 + \alpha\left(-\beta L_r\right)^m\right] \qquad (16)$$

where K_{mat} is the fracture toughness of a high constraint specimen and K^c_{mat} is the fracture toughness at a reduced constraint level. Since no constraint-modified toughness data was available the Wallin T-stress correlation was applied, using T-stress values obtained from the NRI analysis. Figure 42 shows the resulting FAD, which suggests that for the present approximate analysis and the margins on constraint-modified assessments look a little slim.

5.2.3 Two-Parameter Models for Constraint-Based Fracture Assessment

Two-parameter models have been developed to allow the measure of crack tip constraint in term of T-stress, Q or Q_H to be systemically included in fracture assessment. In this project although a number of partners calculated constraint parameters, no two-parameter analysis results were reported. However NRI has separately published the results of an analysis using the K-effective procedure [5] developed by Wallin [17], which integrates the value of K_J over the crack front as well as allowing for a T-stress constraint-loss effect.

[5] The exponent "m" should not be confused with the Weibull shape parameter, also denoted as m.

Using K_{Ieff} produced relatively good accordance between the obtained K_{Ieff} - values and Master Curve predictions made for experimentally determined values of T_0. The analysis indicated that initiation of cleavage fracture is more probable to occur first at the lower crack front, mainly for specimens that exhibited 1st pop-in (or sudden fracture through) at higher loads. This would agree with the limited data from fast video camera records taken during some of tests.

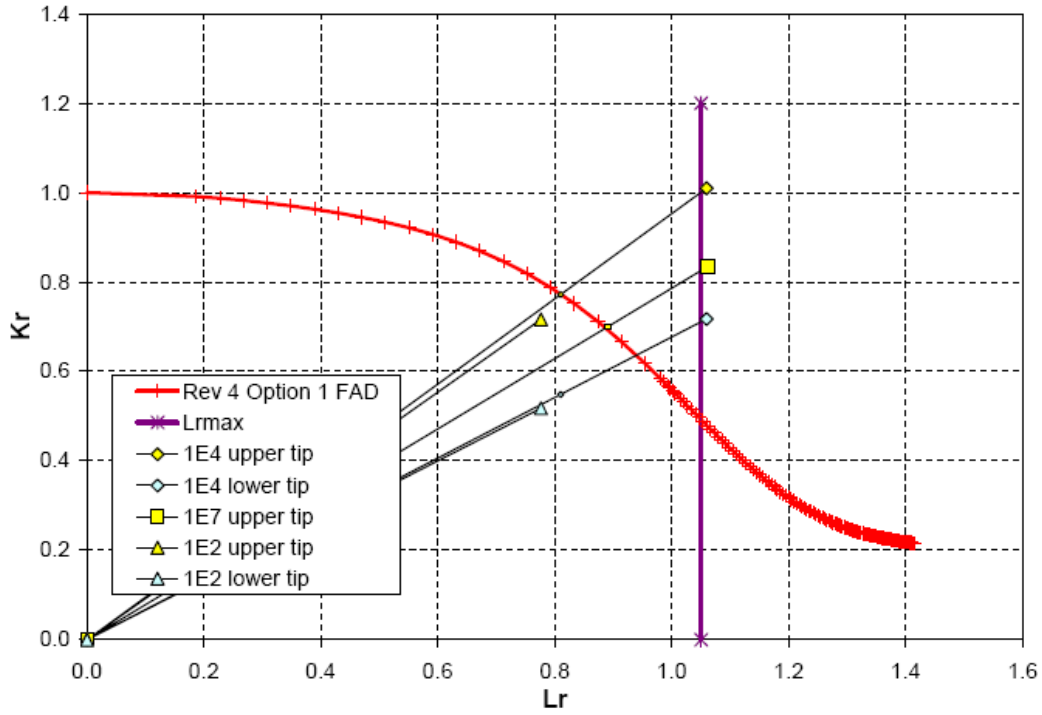

Figure 41 Standard R6 FAD analysis (plane stress).

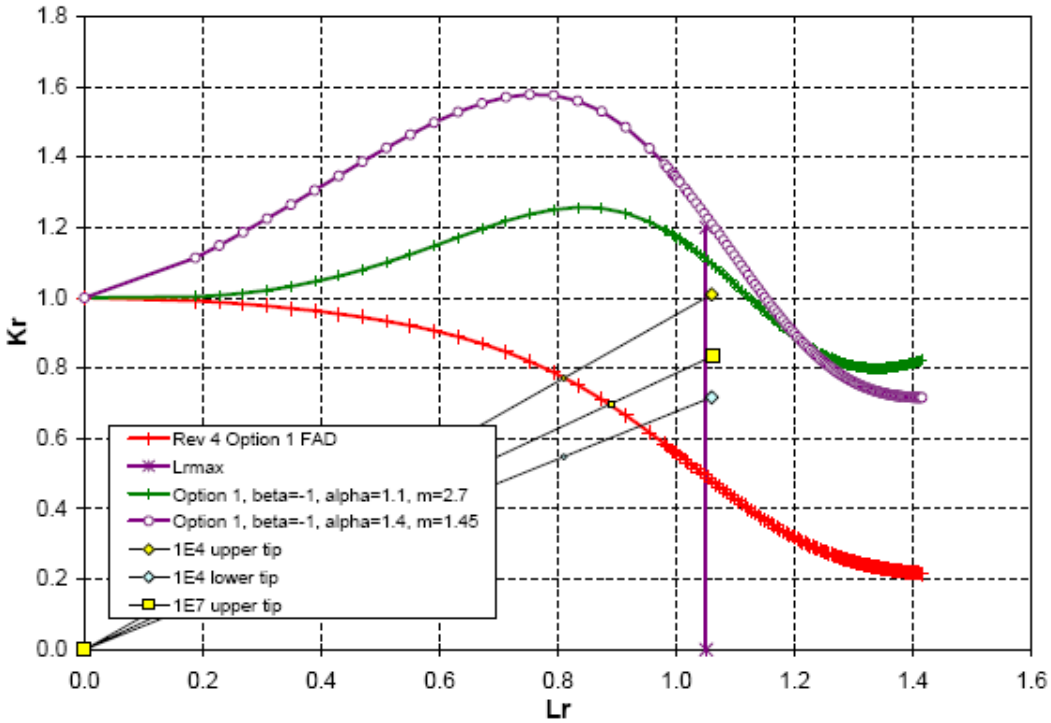

Figure 42 Constraint modified R6 FAD analysis for 1E4 and 1E7.

5.3 Local Approach Models for Brittle Fracture Initiation

5.3.1 ORNL Analysis

Figure 43 and Figure 44 show fracture initiation probability plots for specimens1E2 and 1E7 together with experimental points.[6] For the "normal" specimen (1E2) it is clear to see that the deep crack tip initiates first. For the "abnormal" specimen (1E7), the deep crack tip was blunted, therefore the results shown in Figure 44 cannot be interpreted in a manner that deep tip is more likely to initiate first, if the specimen fails at low load (as would be the case if both crack tips were sharpened).

5.3.2 AREVA GmbH Analysis

AREVA GmbH confined their study to the "normal" beam (1E2). In Figure 45 the rank ordered experimental data (filled triangles) is compared with the predicted failure probability, denoted by the red (lower crack) and blue (upper crack) line. The prediction shows that the crack tip with the lower constraint failed prior compared to the higher constrained crack tip and the predicted probabilities are in very good agreement with the experimental data. It is also visible that the failure curves for the upper and lower crack intersect at a load of about 200kN, so that when this type of beam fails at the lower loading, the shallow crack tip is predicted to initiate first, while the deep crack tip initiates first if the specimen fails at higher loading.

5.3.3 Summary

The results of the two applications of local approach models are in agreement. A comparison of cleavage fracture initiation probability plots for specimen 1E2 is shown in Figure 46, together with the "experimental points" corresponding to the load level at which the first pop-in occurred. Both groups predicted a higher probability that the lower crack front would initiate first than compared to the upper crack front over almost the whole loading range. Only for small loads did Areva predict higher probability of first initiation occurring from the upper crack front. This result is consistent with experimental observations performed via using high speed video camera for some of PHARE experiments [4], [6]. It is also in qualitative accordance with result obtained by NRI Řež (using K_{Ieff} – approach with a T-stress constraint correction) indicating that for those specimens for which the initiation of cleavage fracture occurred at higher loads, it was more likely that the initiation started at the lower crack front [3], [5].

A fully calibrated model could potentially provide more accurate predictions, if sets of fracture toughness data for different constraint condition were available. However ORNL checked the sensitivity of the predictions to the Weibull shape parameter for m=10 and 20 (the baseline value used in the above analyses was 15). The results are summarized in Figure 47 for both crack tips of the "normal"

[6] In the ORNL analysis it was considered more appropriate to compare the predicted probability of fracture P_f under the same bending moment instead of the same driving force. The fracture toughness data K_J was therefore converted to a corresponding bending moment using a polynomial approximation of the driving force vs. bending moment curve.

specimen and show that P_f is almost insensitive to the variation in m. In case of the "abnormal" specimen with the bigger embedded flaw, as presented inFigure 48, P_f is slightly more sensitive, increasing somewhat with increasing m.

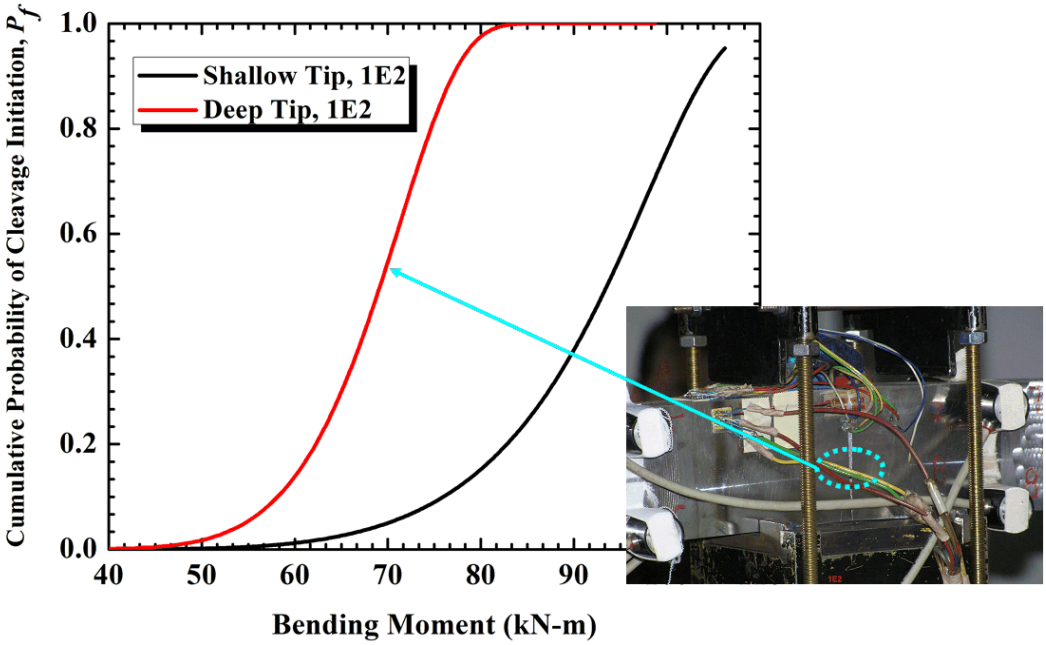

Figure 43 ORNL LA Model: predicted cumulative failure probability for the shallow and deep crack tips of the "normal" specimen (1E2).

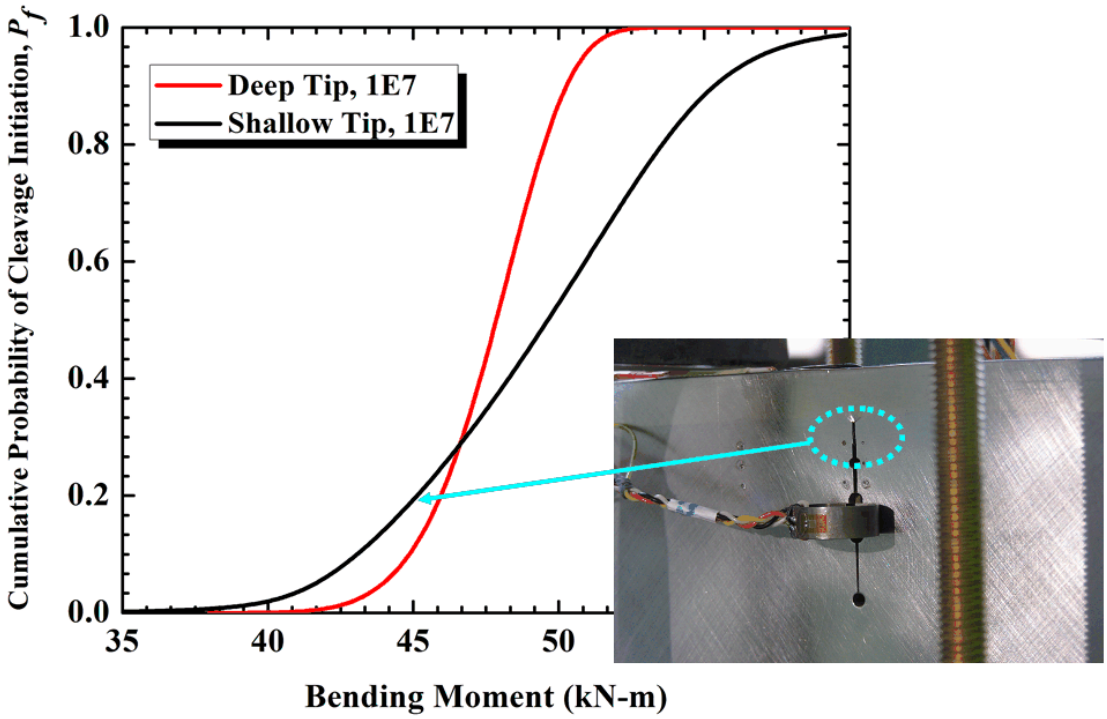

Figure 44 ORNL LA Model: Predicted cumulative failure probability of the shallow and deep crack tips of the "abnormal" specimen (1E7).

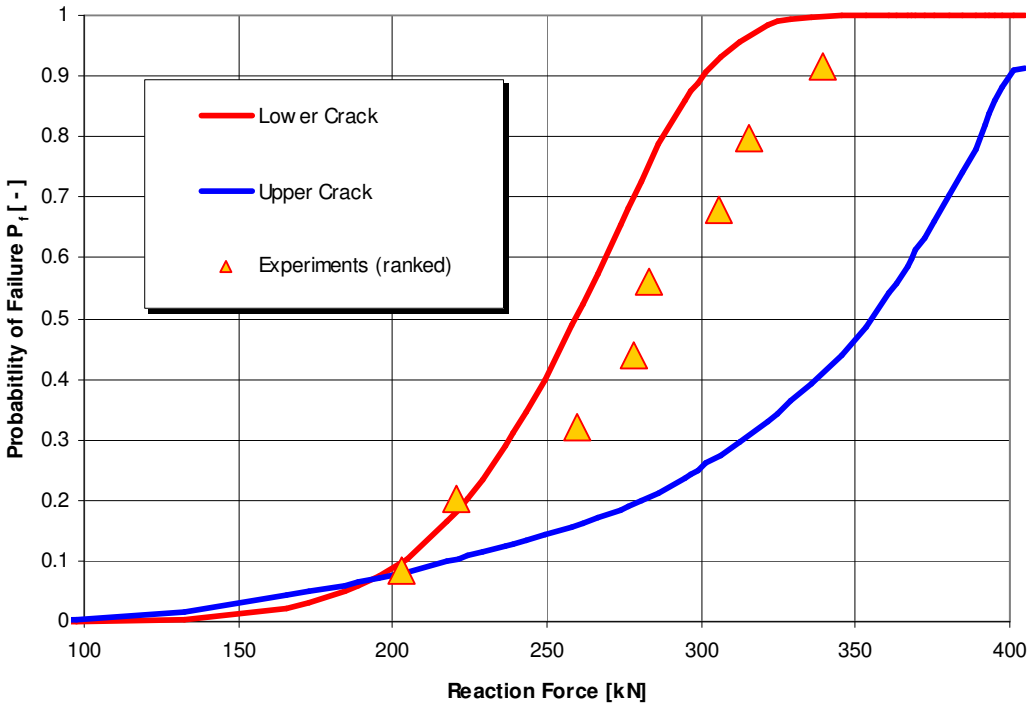

Figure 45 Failure probabilities for the NESC –VI beam from the AREVA LA model.

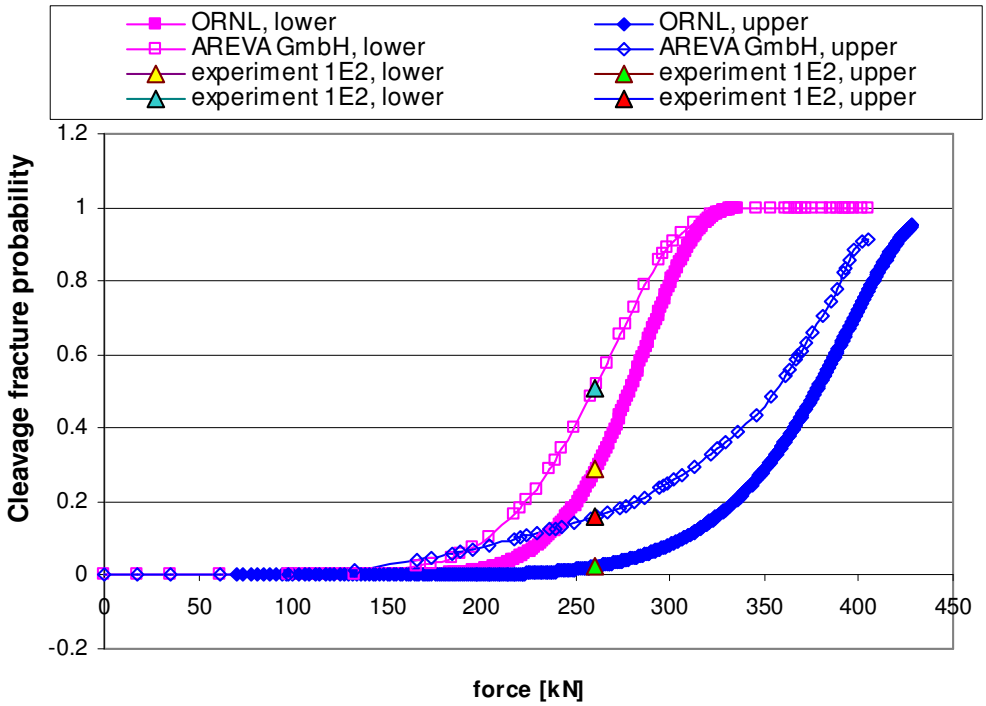

Figure 46 Comparison of the AREVA and ORNL predictions of cleavage fracture probability for test 1E2.

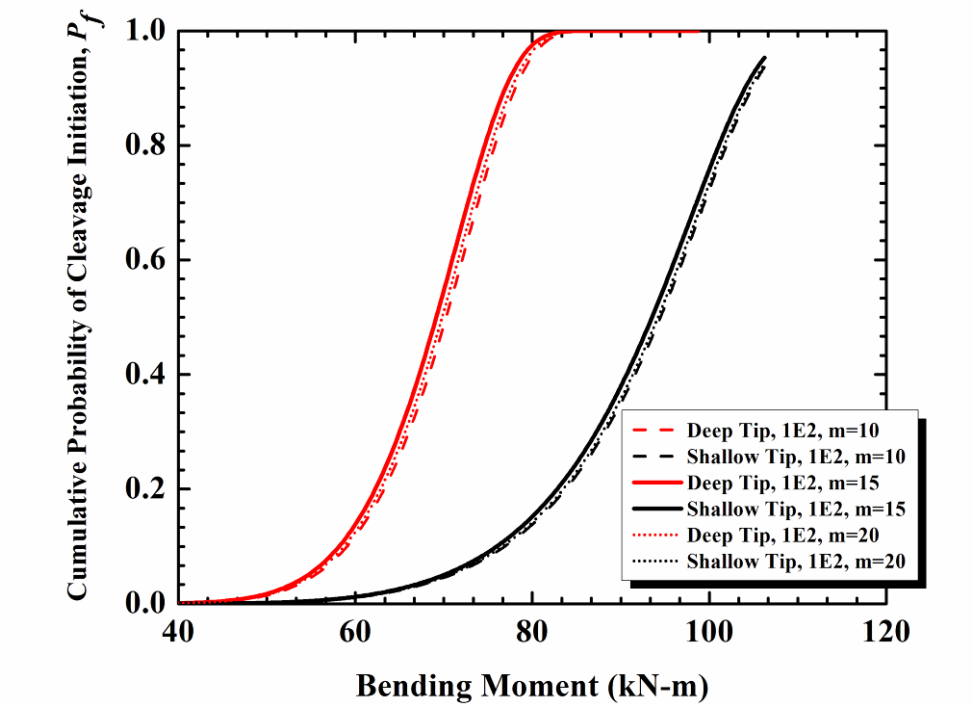

Figure 47 ORNL LA Model: sensitivity of predicated cumulative failure probability with different Weibull modulus, m (1E2).

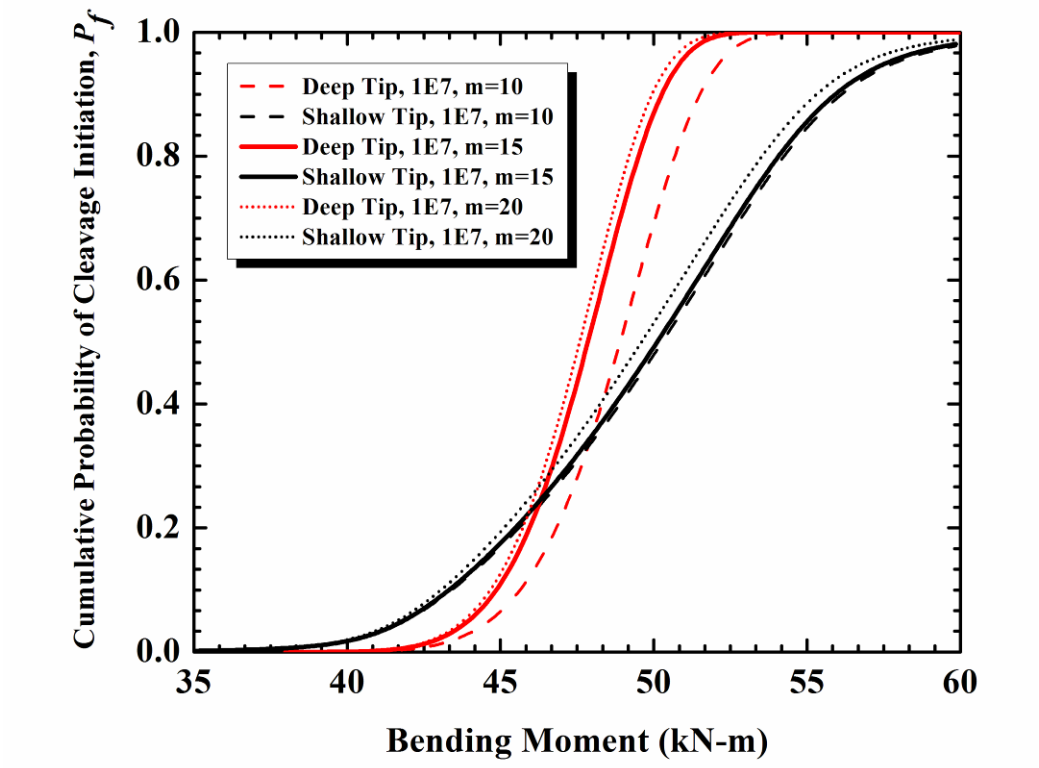

Figure 48 ORNL LA Model: sensitivity of predicated cumulative failure probability with different Weibull modulus, m (1E7).

5.4 Prediction of Crack Arrest in the Cladding

One of the original objectives of the project was to assess the capability to predict whether the cracks propagating into the cladding arrest or cause full fracture. NRI performed extensive FE simulations of observed pop-ins (Figure 49) for the entire set of PHARE tests. These form part of the supporting material for a proposal to update the VERLIFE Unified Procedure, whereby a sub-surface RPV flaw can be postulated in such a manner that it penetrates 1 mm into cladding. For assessment of the crack front lying in cladding the J-integral is evaluated and compared with J_{1mm} value defined on the basis of a conservative J-R curve.

The IWM analysis performed for NESC-VI confirmed that the arrest in the cladding of test 1E2 can be explained from comparison of the J-integral of the arrested crack with the J-R curve. However the break-through of test 1E4 cannot be explained (according to IWM) since the FE analysis predicted crack arrest in the cladding, although at higher J values than for 1E2.

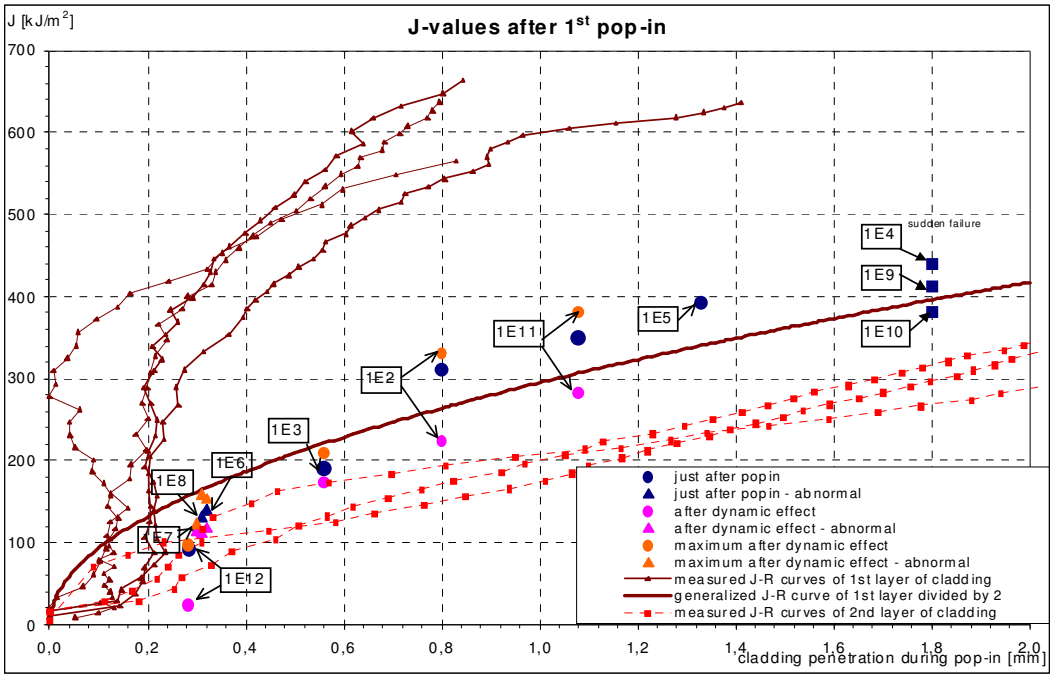

Figure 49 NRI analysis for the J-values in the moment of crack arrest in the cladding after the first pop-in.

6 CONCLUSIONS AND RECOMMENDATIONS

The main results of the project are as follows:

- Comparison of analyses performed by individual partners showed that the FE simulations produced consistent predictions of the observed force vs. load-line displacement (or crack mouth opening displacement) behaviour. However, the differences in crack tip stress intensity values as a function of applied loading were greater than that found in similar intercomparisons in previous NESC projects. This underlines the importance of periodically performing such exercises.

- The influence of two modelling factors on K_J was clearly established: firstly for this type of specimen (for which the clad makes up almost 12% of the cross-section) the clad residual stresses have a significant effect in reducing K_J values and therefore need to be considered in "best-estimate" analysis. The second concerns the use of 2-D or 3-D models: in this case the 2D FE models underestimated K_J values and are considered non-conservative.

- For this combination of test specimen geometry and flaw, constraint loss is expected at the near-surface tip. A range of constraint parameters were evaluated (elastic T-stress, elastic-plastic T-stress and Q) to confirm this. However only in two cases were these used in quantitative way: one constraint-modified FAD assessment and a K_{Ieff} analysis, both using a T-stress parameter. The results show that fracture initiation is more likely at the lower (deep) tip, which is consistent with the limited high-speed video camera evidence. In general a more systematic application of 2-parameter approaches is needed.

- Both local approach models predicted initiation of cleavage fracture first from the lower crack front for medium and higher loads.

Concerning the objective to assess capability to predict whether the cracks propagating into the cladding arrest or cause full fracture, the two analyses performed indicate that when the load at first pop-in is low, crack arrest in the clad can be correctly predicted on the basis of the J-R curve. However further work is needed to ensure the reliability of such approaches over the full load range.

ACKNOWLEDGEMENTS

This report is a synthesis of a collective effort of an international team of experts. Very sincere thanks are due to all those persons and organisations who contributed to the project, for the most part on a contribution-in-kind basis. The following list hopefully leaves no one out: M. Brumovsky (NRI), D. Lidbury (Serco Assurance), E. Keim and M. Hümmer (Areva NP GmbH), S. Szabolcs and R. Beleznai (Bay Zoltan), H. Keinanen (VTT), D. Siegele (IWM), M. Smith (British Energy), C. Malekian (Tractebel), I. Sattari-Far (Inspecta), K. Wallin (VTT), S. Yin and R. Bass (ORNL).

REFERENCES

[1] IAEA-TECDOC-1120, Assessment and management of ageing of major nuclear power plant components important to safety: PWR pressure vessels, IAEA, 1999.

[2] Simonen, F.A., Schuster, G.J., Doctor, S.R., Dickson, T.L., Distributions of fabrication flaws in reactor pressure vessels for structural integrity evaluations , American Society of Mechanical Engineers, Pressure Vessels and Piping Division (Publication) PVP, 443 (2), pp. 133-143, 2002.

[3] Lauerova, D., Pistora, V., Kacor, A., Brumovsky, M., Evaluation of constraint in semi-large scale experiments performed on specimens with underclad cracks, 19th Int. Conf. on Structural Mechanics in Reactor Technology (SMiRT-19), Toronto, 2007.

[4] Pistora, V., Brumovsky, M., Kohopaa, J., Lauerova, D., Wallin, K., Semi-large scale experiments performed on specimens with underclad cracks, 19th Int. Conf. on Structural Mechanics in Reactor Technology (SMIRT 19), Toronto, 2007.

[5] Lauerova, D., Brumovsky, M., Evaluation of experiments on semi-large scale specimens with underclad cracks with focus on constraint evaluation, ASME PVP 2008 Conference, Chicago, 2008.

[6] Pistora, V., Brumovsky, M., Semi-large scale experiments performed on specimens with underclad cracks, ASME PVP 2008 Conference, Chicago, 2008.

[7] Taylor, N., Lidbury, D., Improving structural integrity assessment techniques, 1st Symposium - Nuclear Pressure Equipment Expertise and Regulation, International Conference, Dijon, 2005.

[8] Debarberis, L., Role of international networks on structuring nuclear safety research and disseminating results, Proc. FISA 2003, EUR 21026, 2004.

[9] Rintamaa, R., Aho-Mantila, I., Taylor, N., NULIFE - European network dedicated to nuclear plant life management, American Society of Mechanical Engineers, Pressure Vessels and Piping Division (Publication) PVP, 6, pp. 217-224, 2008.

[10] Bass R., Wintle J., Hurst R.C., Taylor N., NESC-I project overview, European Commission Report EUR 19051EN, 2001.

[11] Stumpfrock L. et al, NESC-II Final Report, European Commission Report EUR 20696 EN, 2003.

[12] Taylor, N., Faidy, C., Gilles, P., Integrity of dissimilar metal welds – Final Report of the NESC-III Project, European Commission Report EUR 22510 EN, 2006.

[13] Taylor, N. et al, NESC-IV Project: An investigation of the transferability of Master Curve technology to shallow flaws in reactor pressure vessel applications, European Commission Report EUR 21846 EN, 2005.

[14] Taylor, N., Nilsson, K.F., Dahlberg, M., Faidy, C., A procedure for thermal fatigue damage assessment due to turbulent mixing in nuclear piping systems, Proc. Int. Conf. "Fatigue Design", Senlis, 2005.

[15] NESC-VI data pack.

[16] Taylor N., et al, Use of Master Curve technology for assessing shallow flaws in a reactor pressure vessel material, accepted for publication in ASME J. Pressure Vessel Technology, 2008.

[17] Wallin, K., Rintamaa, R., Use of the Master Curve methodology for real three-dimensional cracks, 18th International Conference on Structural Mechanics in Reactor Technology (SMiRT 18), Beijing, 2005.

[18] R6 procedure rev 4, section 3.7, 2001.

[19] Beremin, F., A local criterion for cleavage fracture of nuclear pressure vessel steel, Metallur. Trans., 14A, 2277-2287, 1983.

[20] Ruggieri, C., Dodds, R. Jr., WSTRESS 2.0, Numerical Computation of Probabilistic Fracture Parameters, UILU-ENG-95-2013, University of Illinois at Urbana-Champaign, 1998.

[21] Hümmer M., Keim E., Hofmann H., TIMES: An international project on transferability of fracture toughness values for irradiated RPV steels, Proceedings of the PVP, ASME Pressure Vessels and Piping Division Conference, San Antonio, 2007.

[22] Standard test method for determination of reference temperature, T_0, for ferritic steels in the transition range," E 1921-2002, Annual Book of ASTM Standards Section 3: Metals Test Methods and Analytical Procedures, Vol. 03.01 Metals – Mechanical Testing, Elevated and Low-Temperature Tests, Metallography, American Society for Testing and Materials, 2002.

[23] Morgan, B., Applied stochastic modeling, Oxford University Press, 2000.

[24] Gao, X., Ruggieri, C., Dodds, R. H., Calibration of Weibull stress parameters using fracture toughness data, International Journal of Fracture 92, 175-200, 1998.

[25] Pistora V. et al, Large scale cladded beam specimen tests, description of the project for NESC, Report NRI Rez, 2007.

[26] ABAQUS/Standard User's Manual, Version 6.7.1. ABAQUS Inc., 2006.

[27] Dodds, R., Anderson, T., Kirk, M., A framework to correlate a/W ratio effects on elastic-plastic fracture toughness (J_c), International Journal of Fracture, Vol. 48, pp. 1-22, 1991.

[28] Lidbury, D.P.G, Sherry, A.H., Bass, B.R., Gilles, P., Connors, D., Eisele, U., Keim, E., Keinanen, H., Wallin, K., Lauerova, D., Marie, S., Nagel, G., Nilsson, K.-F., Siegele, D., Wadier, Y., Validation of constraint-based methodology in structural integrity of ferritic steels for nuclear reactor pressure vessels, Fatigue Fract. Engng. Mater. Struct., 29, 1-21, 2006.

[29] Betegon, C. and Hancock, J., Two parameter characterisation of elastic-plastic stress fields, J. Appl. Mech., 58(1), pp.104-110, 1991.

[30] Sumpter, J., Hancock, J., Status review of the J plus T stress fracture analysis method, Proc. European Conference on Fracture 10, EMAS, 1994.

[31] O'Dowd, N., Shih, C., Family of crack tip fields characterised by a triaxiality parameter: part I – structure of fields, J. Mech. Phys. Solids, Vol. 39, pp. 989-1015, 1991.

ANNEX A - Fractography of fracture surfaces

Part I: Brief fractography analysis

Specimen 1E2 – Overall view on upper part of the crack

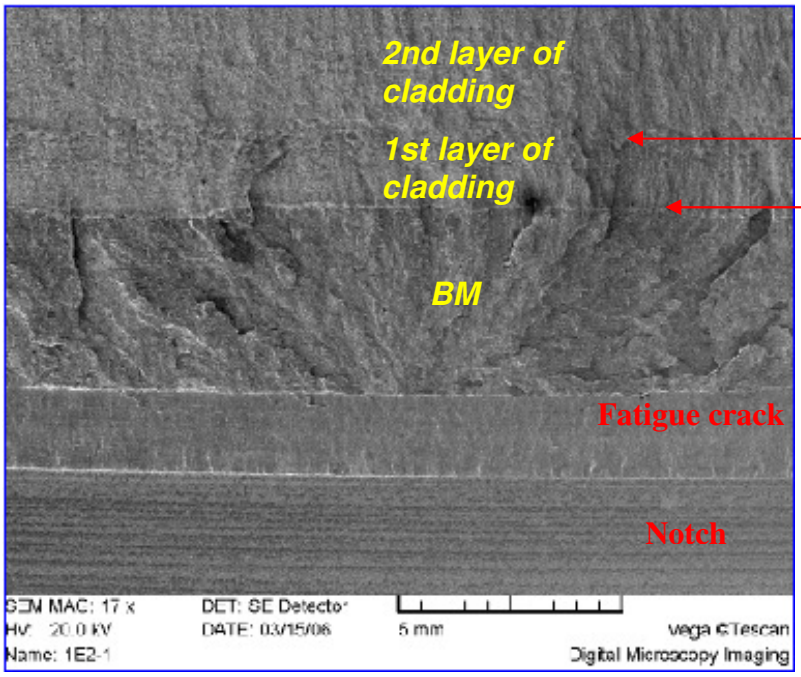

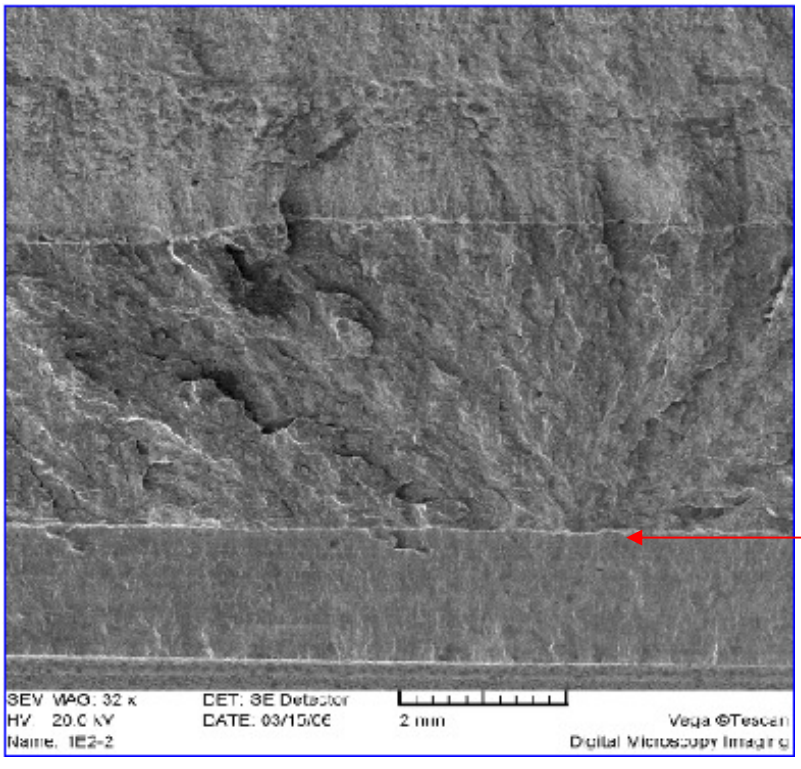

Specimen 1E2 – Blunting zone between fatigue crack and cleavage region

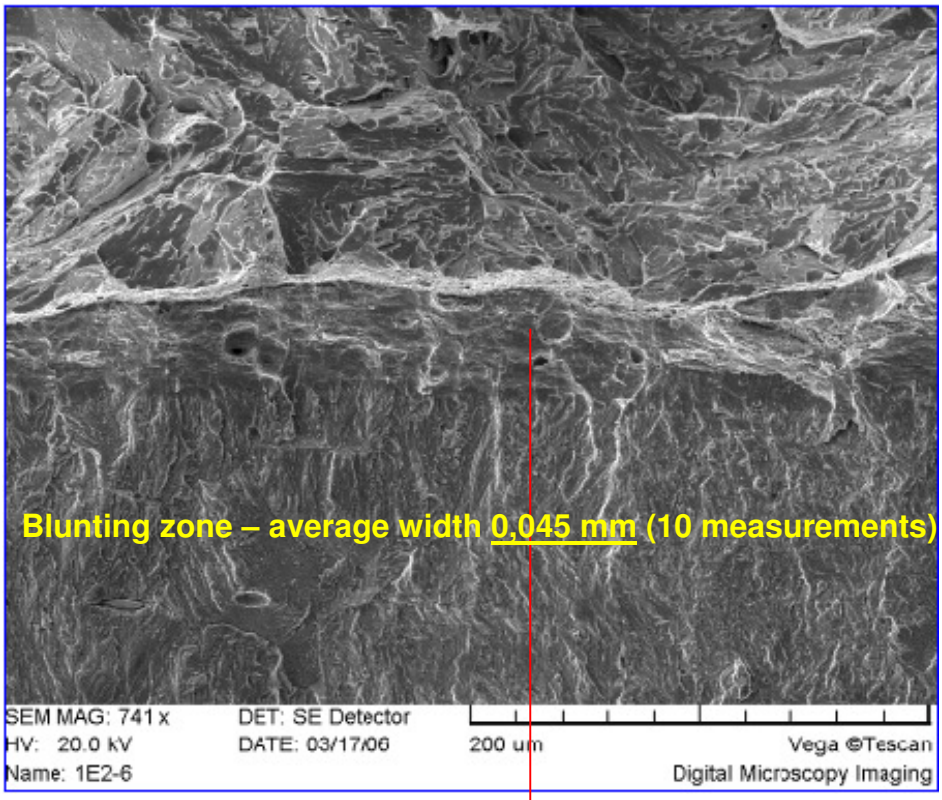

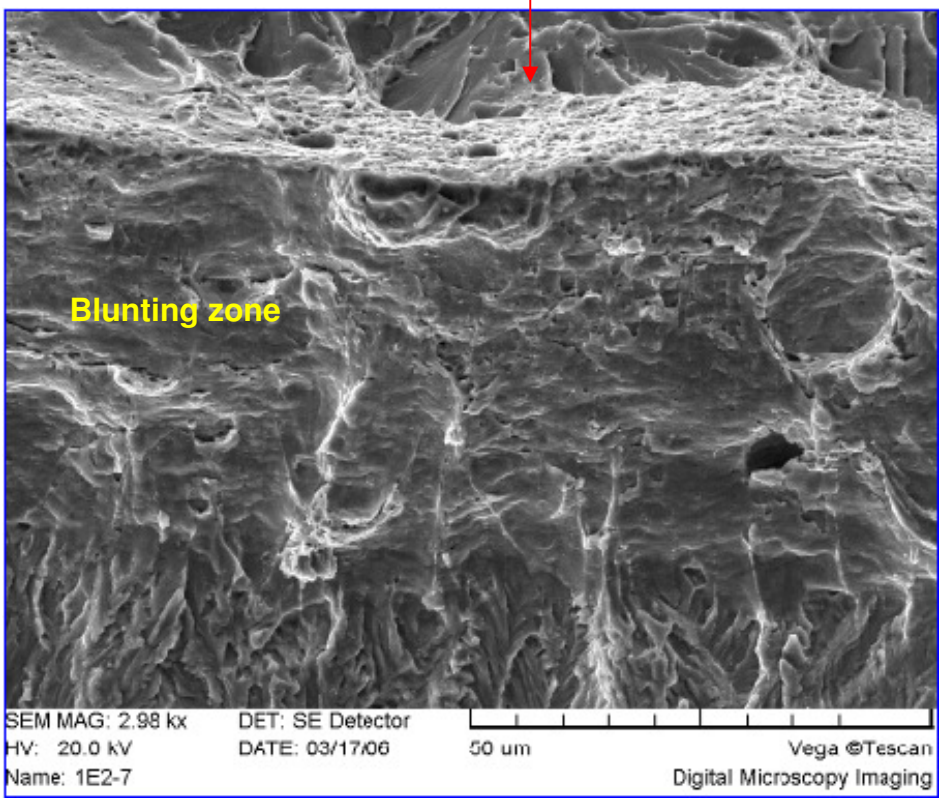

Part II: Fractography – summary

Type of material	Structure	Chemical composition*	6.1.1.1 Region	6.1.1.2 Type of fracture				
				Fatigue	B-TG	B-IG	D-IG	D-TG
2nd layer of cladding	Dendritic – weld metal	Cr, Ni, Nb, Mn - austenite	D_3					+
1st layer of cladding	Dendritic – weld metal	Cr, Ni, Mn, Al - austenite	$D_1 + D_2$					+
Base material	Bainitic	Cr,Mn,V - steel	$C_1 + C_2$	+	+	+	+	
Instrumented notch								
Base material	Bainitic	Cr,Mn,V - ocel	$B_{1-3} + A$	+	+			

Abbreviations	
B-TG	Brittle transgranular fracture
B-IG	Brittle intergranular fracture
D-IG	Ductile intergranular fracture
D-TG	Ductile transgranular fracture

European Commission

EUR 23968 EN – Joint Research Centre – Institute for Energy
Title: Benchmark Analyses for Fracture Mechanics Methods for Assessing Sub-Clad Flaws
Authors: D. Lauerova, N. Taylor, V. Pistora, P. Minnebo, E. Paffumi

Luxembourg: Office for Official Publications of the European Communities 2009
EUR – Scientific and Technical Research series - ISSN 1018-5593

Abstract

The sixth project of the Network for Evaluating Structural Integrity (NESC-VI) deals with the fracture mechanics analysis of a set of 3 tests on beam specimens with simulated sub-surface flaws, which were performed by NRI Řež plc for the PHARE project "WWER Cladded Reactor Pressure Vessel Integrity Evaluation (with Respect to PTS Events)". The objectives were as follows:

- to assess the capability to predict whether the cracks propagating into the cladding arrest or cause full fracture, and
- to assess the capability to predict the location of first initiation: near-surface or deep crack tip.

The project was launched in December 2006 and completed in March 2009. It brought together a group of 10 organisations from NESC to perform comparative analyses of selected tests, based on a comprehensive data-pack prepared by NRI. The investigations focussed almost exclusively on assessing the capability to predict the location of first initiation. The main results are as follows:

- Comparison of analyses performed by individual partners showed that the FE simulations produced consistent predictions of the observed force vs. load-line displacement (or crack mouth opening displacement) behaviour. However the differences in predicted crack tip stress intensity, K_J, as a function of applied loading were greater than those found in similar intercomparisons made as part of previous NESC projects. This underlines the importance of periodically performing such exercises.
- The influence of two modelling factors on K_J was clearly established: firstly for this type of specimen, for which the clad makes up almost 12% of the cross-section, the associated residual stresses have a significant effect in reducing K_J values and therefore need to be considered in "best-estimate" analysis. The second concerns the use of 2-D or 3-D models: in this case the 2D FE models underestimated K_J values and are considered non-conservative.
- For this combination of test specimen geometry and flaw, constraint loss is expected at the near-surface tip. A range of constraint parameters were evaluated (elastic T-stress, elastic-plastic T-stress and Q) to confirm this. However only in two cases these were used in quantitative analyses: constraint-modified FAD and K_{Ieff}, both using elastic T-stress. These indicate that fracture is likely to initiate at lower (deep) tip, which is consistent with the limited high-speed video camera evidence. In general more systematic application of 2-parameter approaches is needed.
- Both local approach models predicted initiation of cleavage fracture first from the lower crack front for medium and higher loads.

Concerning the capability to predict whether the cracks propagating into the cladding arrest or cause full fracture, the two analyses performed indicate that when the load at first pop-in is low, crack arrest in the clad can be correctly predicted on the basis of the J-R curve, but that further work is needed to ensure the reliability of such approaches over the full load range.

The mission of the JRC is to provide customer-driven scientific and technical support for the conception, development, implementation and monitoring of EU policies. As a service of the European Commission, the JRC functions as a reference centre of science and technology for the Union. Close to the policy-making process, it serves the common interest of the Member States, while being independent of special interests, whether private or national.